



Norwegian University of
Science and Technology

Objective Image Quality Metrics for Ultrasound Imaging

Cecilie Øinæs Simpson

Master of Science in Electronics

Submission date: June 2009

Supervisor: Ilangko Balasingham, IET

Co-supervisor: Hans Torp, ISB
Sten Roar Snare, ISB

Problem Description

Last 10-15 years, the development in the field of medical ultrasound has led to advanced imaging equipment with impressive real time images of for instance the unborn, the heart, liver and other organs. With the increasing complexity of the equipment, a challenge is to keep the systems as user friendly as possible. An important part of this work is the task of automatic image optimization. An important prerequisite for automatic image optimization is the ability to objectively measure image quality. Ultrasound images suffer from speckle noise and aberrations. Many of the common quality measures from photography and other imaging modalities may not be suitable at all. Objective measurement of ultrasound image quality is not a trivial task.

During a summer job at GE Vingmed and during her project work at NTNU the autumn 08, Cecilie Simpson has made a framework for measuring ultrasound image quality on tissue mimicking phantoms. The system evaluates point targets and cysts in phantom images and objectively describes characteristics related to image quality. It has been extended to support simulated (Field II) data and to work within the Matlab environment. Emphasis has been on the point spread function (PSF) and simple contrast to noise (CNR) measures. The simulation framework will allow extensive virtual testing of parameters.

During her work with the master thesis, Cecilie will work to extend the analysis software to support new parameters, in addition to the current PSF and CNR measurements.

Cecilie will also work to incorporate the ProbeContact algorithm in her measurement system. ProbeContact is an algorithm developed at ISB. It provides the user with real time feedback whether the ultrasound probe has the required contact surface with the skin or not. This will allow for experimental testing of Probe Contact, hopefully with accompanying objective image quality measures.

Assignment given: 15. January 2009
Supervisor: Ilangko Balasingham, IET

Abstract

Objective evaluation of the image quality on ultrasound images is a comprehensive task due to the relatively low image quality compared to other imaging techniques. It is desirable to objectively determine the quality of ultrasound images since quantification of the quality removes the subjective evaluation which can lead to varying results. The scanner will also be more user friendly if the user is given feedback on the quality of the current image.

This thesis has investigated in the objective evaluation of image quality in phantom images. It has been emphasized on the parameter spatial variance which is incorporated in the image analysis system developed during the project assignment. The spatial variance was tested for a variety of settings as for instance different beam densities and number of MLAs. In addition, different power spectra have been evaluated related to the ProbeContact algorithm developed by the Department of Circulation and Medical Imaging (ISB). The algorithm has also been incorporated in the image analysis system.

The results show that the developed algorithm gives a good indication of the spatial variance. An image gets more and more spatially variant as the beam density decreases. If the beam density goes below the Nyquist sampling limit, the point target will appear to move more slowly when passing a beam since the region between the two beams are undersampled. This effect will be seen in the correlation coefficient plots which is used as a measure of spatial variance.

The results from the calculations related to the ProbeContact algorithm show that rearranging the order of the averaging and the Fourier transformation will have an impact on the calculated probe contact, but the differences are tolerable. All the evaluated methods can be used, but performing Fourier transform before averaging can be viewed as the best solution since it gives a lateral power spectrum with low variance and a smooth mean frequency and bandwidth when they are compared for several frames. This is suggested with the reservations of that basic settings are used. Performing 1D (in the lateral direction) or 2D Fourier transform before averaging will not have any impact of the resulting power spectrum as long as normalized Fourier transform is used.

The conclusion is that the image analysis system, including the spatial variance parameter, is a good tool for evaluating various parameters related to image quality. The system is improved by the ProbeContact algorithm which gives a good indication of the image quality based on the acoustic contact of the probe. Even though the image analysis system is limited to phantom images, the thesis is a starting point in the process of obtaining objective evaluation of the image quality in clinical images since others may use it as a basis for their work.

Preface

This thesis is the result of the master assignment "Objective Image Quality Metrics for Ultrasound Imaging". The thesis is a part of the Master of Science program at the Department of Electronics and Telecommunications at the Norwegian University of Science and Technology (NTNU). The thesis has been performed during the spring 2009 at the Department of Circulation and Medical Imaging.

I would especially like to thank my supervisor PhD student Sten Roar Snare for very helpful guidance and support. He has been an excellent supervisor. I will also like to thank Professor Hans Torp for valuable suggestions and clarifications, and PhD Lasse Løvstakken for useful help with the ProbeContact algorithm.

Trondheim, June 8, 2009

Cecilie Øinæs Simpson

Contents

1	Introduction	1
1.1	Thesis Outline	2
I	Background	3
2	Ultrasound Theory	5
2.1	Main Principles	5
2.2	B-mode Imaging System	6
2.3	Beam Profile and k-space	7
2.4	Point Spread Function	9
2.5	MLA	10
2.6	Speckle	11
2.7	Phantoms	12
2.8	Image Quality	13
3	Related Theory	16
3.1	Correlation	16
3.2	Spectral Analysis	18
II	Methods and Implementation	21
4	Tools	23
4.1	Scanner Setup	23
4.2	GcMat	23
4.3	Field II	24
4.4	Existing Image Analysis System	24
5	Spatial Variance	25
5.1	Background	25
5.2	Implementation	26
5.3	Methods	27
6	ProbeContact	28
6.1	Background	28
6.2	Implementation and Methods	28

III Results and Discussion	33
7 Results	35
7.1 Spatial Variance	35
7.2 ProbeContact	45
8 Discussion	49
8.1 Spatial Variance	49
8.2 ProbeContact	53
IV Conclusion	55
9 Conclusion	57
9.1 Future Work	58
References	61
V Appendices	63
A Mathematical Relations in ProbeContact	65
A.1 Mathematical Equations Used in the Four Cases	65
A.2 Relation Between Averaging and 1D FT	66
A.3 Relation Between Averaging and $ 1D\ FT ^2$	66
A.4 Relations Between Averaging, $ 1D\ FT ^2$ and $ 2D\ FT ^2$	68
B GUI for Image Analysis System	71
C Movie of Point Target	74
D Correlation Coefficient Calculations for IQ-data	75

List of Figures

2.1	Reflection and transmission of a pulse between mediums	5
2.2	B-mode imaging system	6
2.3	Radiation of a beam	7
2.4	Transducer geometry and corresponding directions	8
2.5	K-space responses.	9
2.6	The point spread function (PSF)	9
2.7	PSF in k-space	10
2.8	MLA	11
2.9	Phantom CIRS40	12
3.1	Template matching	18
4.1	Recorded image with five frames in existing image analysis system	24
6.1	The four different cases related to the ProbeContact algorithm . .	29
7.1	Correlation coefficient for the recorded images	36
7.2	Correlation coefficient for the simulated images	37
7.3	Correlation coefficient for the simulated images with different distance calculation	38
7.4	Lateral profiles for the simulated images with 81 and 19 beams . .	38
7.5	Correlation coefficient calculated from beamspace tissue data and from IQ-data for a simulated image with 48 beams	39
7.6	Correlation coefficient calculated from beamspace tissue data and from IQ-data for a simulated image with 24 beams	39
7.7	Correlation coefficient for the recorded images with speckle ROI .	40
7.8	Correlation coefficient for the simulated images with speckle ROI .	41
7.9	Correlation coefficient for the simulated images calculated from IQ-data with speckle ROI	41
7.10	Correlation coefficient for three point targets in the recorded images	42
7.11	Correlation coefficient for three point targets in the simulated images	42
7.12	Correlation coefficient for the scanned images with 2 and 4 MLA .	43
7.13	Correlation coefficient for the simulated images with 2 and 4 MLA	43
7.14	Correlation coefficient for the simulated images with different distance calculation and with 2 and 4 MLA	44
7.15	Lateral minimum and maximum profiles for the scanned and simulated image with 4 MLA	44
7.16	Lateral power spectrum for the four cases in addition to a lateral power spectrum of N times case 3	45
7.17	Lateral power spectrum for the four cases, normalized DFT	46

7.18	2D power spectrum together with lateral and radial spectrum . . .	46
7.19	Power spectrum map for the four cases	47
7.20	Mean frequency and bandwidth with increasing frame number for the four cases.	48
B.1	First menu that appears when running menuSystem.m	71
B.2	Second menu that appears when running menuSystem.m	72
B.3	Menu with options related to calculations of the spatial variance .	73

List of Tables

4.1	Scanner settings	23
7.1	Distance between transmit beams and Nyquist sampling limit . . .	37
7.2	Calculated mean frequency and bandwidth for the four cases in ProbeContact	47
A.1	DFT and average definition(s)	65

Chapter 1

Introduction

In medical ultrasound, images of soft tissue and blood flow are obtained for medical diagnosis purposes. This imaging method is popular since ultrasound is a non-invasive method with real time recordings, and it is relatively inexpensive compared to other medical equipment. In addition, the ultrasound scanner is getting smaller and more mobile. A downside of ultrasound is that the image quality is not as good as other medical imaging methods as for instance Magnetic Resonance Imaging (MRI) and Computer Tomography (CT). While these imaging techniques have clear edges and a low amount of noise, ultrasound images often consist of the opposite. They include a lot of speckle noise, and the images are clearly blurry in comparison to these methods. Objective measurement of ultrasound image quality is accordingly not a trivial task.

The evaluation of image quality by computerized image analysis has existed for many years on photographs. It has also been tried for instance on MRI and CT images. But there exist no published methods to date which objectively evaluate the quality of clinical ultrasound images. However, there have been developed some programs for performance testing on ultrasound scanners, and many of the used methods are closely related to image quality metrics. A disadvantage of these programs is that they all require more or less user interaction, and in some cases the images must be recorded several times.

A system that objectively evaluates the image quality is desirable for several reasons. As the ultrasound equipment gets more complex, it is important that the scanners maintain user friendly. More complexity leads to fewer people with enough education to handle the equipment in a way that the best image quality always will be obtained. When, in addition, the ultrasound scanners are getting smaller, the scanners will be introduced to new areas like a local doctor office and not in a hospital with trained sonographers. It will then be increasingly important to have a system that can give the user feedback on the quality of the current image.

The purpose of this study has been to objectively evaluate the image quality of phantom images. During the summer job at GE Vingmed Ultrasound and during the project work the autumn 2008, a framework for measuring ultrasound image quality on phantom images was made [20]. This image analysis system evaluates point targets and cysts in the image and objectively describes their characteristics related to image quality. In this thesis, the image analysis system has been further developed by evaluating the spatial variance in

images. Spatial variance is an important parameter related to image quality since it gives a good indication of whether objects will be displayed equally in all parts of the image. The spatial variance was tested both for recorded and simulated images, and also by changing different variables as for instance different beam densities and the number of MLAs.

In addition, the ProbeContact algorithm has been incorporated in the system. The algorithm is developed by the Department of Circulation and Medical imaging (ISB) and provides the user with real time feedback of the acoustic contact between the probe and the patient's skin [12]. Poor contact will greatly reduce the quality in the image and ProbeContact is a great tool related to objective evaluation of image quality. The power spectrum determines the acoustic contact of the probe, and an evaluation of different power spectrum calculations will be presented in this thesis.

1.1 Thesis Outline

The thesis is organized as follows.

- Part 1 (Chapter 2-3) describes background information about ultrasound and theory related to the two main topics in this thesis; spatial variance and the ProbeContact algorithm.
- Part 2 (Chapter 4-6) presents tools used in the work together with methods and implementation of spatial variance and of power spectrum calculations in ProbeContact.
- Part 3 (Chapter 7-8) presents the results and the discussion of the findings.
- Part 4 (Chapter 9) concludes the thesis and suggests further work.
- Part 5 (Chapter A-D) contains appendices with more detailed descriptions and mathematical derivations.

Part I

Background

Chapter 2

Ultrasound Theory

Ultrasound is defined as mechanical waves with a higher frequency than humans can hear, that is greater than 20 kHz [9]. Ultrasound is used in several fields as diagnostic, clinical and industrial applications, but the most well known application is its use in diagnostic ultrasound by composing pictures of the fetus in a pregnant woman. This chapter aims to give the reader a brief introduction to some of the principles in diagnostic ultrasound.

2.1 Main Principles

An ultrasound wave is generated by using a piezoelectric plate, i.e. a transducer, which will transmit a pulse into the human body. When a pulse hits a boundary between two tissue structures, some part of the pulse will be reflected and some part will be further transmitted into the body, see Figure 2.1. For each boundary, the pulse will be influenced in some way. If two structures have huge differences in their properties, nearly the whole pulse will be reflected and the echo back to the transducer will be strong. Less differences in the materials properties give weaker echoes. The intensity of the pulse will decrease as the pulse propagates through the tissue, and the reflected signal from far away structures will then be much weaker compared to echoes from close structures. The transducer receives the echoes with different intensities at different times and this is used to detect the locations of the structures. By shooting with many pulses successively in a specific region, an image can be formed.

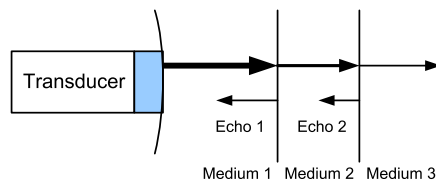


Figure 2.1: The pulse is reflected and transmitted at each boundary between the media. The intensity of the pulse will decrease as the pulse propagates through the tissue. The figure is found in [9].

2.2 B-mode Imaging System

A B(brightness)-mode image displays the geometry of the organ being imaged by use of different brightness levels to show the various strengths of the echoes. Figure 2.2 shows the different signal processing steps in a B-mode imaging system from receiving the transmitted pulses to displaying the processed data on a screen. When the pulses hit the transducer, the received echoes are delayed and summed. The summed signals are called RF-data and consist of unprocessed data.

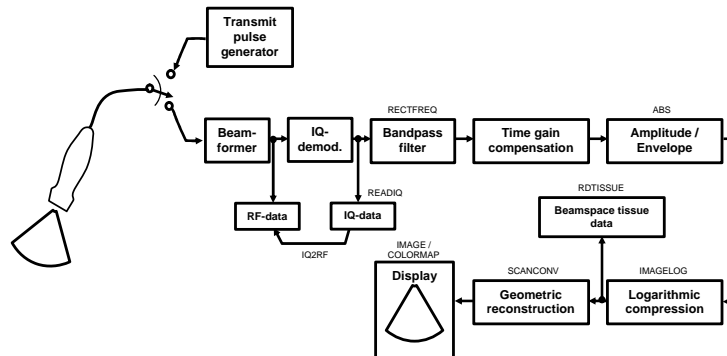


Figure 2.2: A B-mode imaging system. The figure shows the different processing steps from transmitting and receiving the pulses to displaying the result on the screen. The figure is found in [23].

The RF-data is first In-phase Quadrature (IQ) demodulated. IQ-demodulation is a complex base-band modulation technique where the bandpass RF-signal is down-mixed so the resulting signal is complex and a lowpass signal. By applying IQ-demodulation, the amount of data is reduced without losing essential information and a lower sampling frequency can be used [11].

After IQ demodulation, a bandpass filter is applied to maximize the ratio between the signal and the noise. This is done by filtering with a frequency band around the transmitted frequency or twice this frequency.

The next step in the process is Time Gain Compensation (TGC). Due to attenuation, the reflections from structures at far depths are much weaker than reflections at shallow depths. TGC compensates for this intensity drop by gradually amplifying the signal with increasing depth [25].

Next, amplitude and envelope detection are performed on the signal. It is done to rectify and smooth the signal.

To be able to visualize weak echoes together with strong ones, the dynamic range is reduced by applying logarithmic compression on the signal. The data after this processing is called beamspace tissue data.

The last step before displaying the image is geometric reconstruction of the data. This is also called scan conversion, and it converts the signal into a format that is compatible with a specific type of display. When the ultrasound pulses is fired in a sector, it is also desirable to display the image as a sector, and the image must be corrected by displaying the data points close to the probe with a very small distance and displaying data points with increasing distance between each other as we move away from the probe.

2.3 Beam Profile and k-space

An ultrasound beam can be created by shooting one or many pulses in the same direction from the transducer surface, the aperture. The radiation of a beam into the field is shown in Figure 2.3. As can be seen from this figure, the central core of the beam is called the main lobe. The field outside of this region consists of side lobes that have a lower intensity level than inside the main lobe. The side lobes are caused by interference and create artifacts[†] in the image.

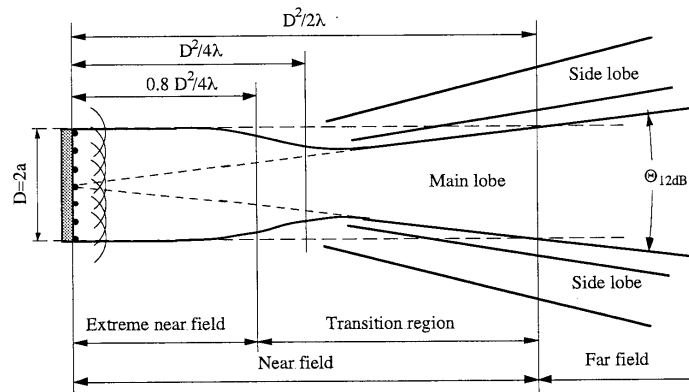


Figure 2.3: The radiation of a beam. The figure shows the main lobe and side lobes of a beam in addition to near and far field. The figure is found in [16].

It is also common to divide the radiating field into the near field and far field. The beam acts differently in the two regions. In the far field, the area of the beam will expand beyond the aperture of the transducer, while in the near field the beam area will be less than the aperture size [25].

The beam profile is defined as the spatial variations of the beam amplitude [16]. It shows how the intensity of the beam varies in the field. The profile can be looked at from several directions. The directions and transducer geometry are illustrated in Figure 2.4. The transducer surface consists of many small elements, and it is possible to both steer and focus the beam by delaying these elements. Doing so will influence the beam profile. The range, or radial, dimension is the direction along the beam where the predominant sound wave propagates from the transducer and into the body. The lateral dimension is the direction across the beam. The radial and lateral dimensions define the 2D plane that is displayed in most B-mode images.

K-space is a frequency domain description in ultrasound imaging systems which can be used to gain insight into the interactions during image formation [26]. K-space representation describes spatial response in the frequency domain and will here be used to explain the connection between the aperture responses and the beam profile.

The response of the transmit aperture and the receive aperture gives together the transmit-receive response which is called the pulse-echo response.

[†]A structure in the image that does not provide a true representation of the scanned object.

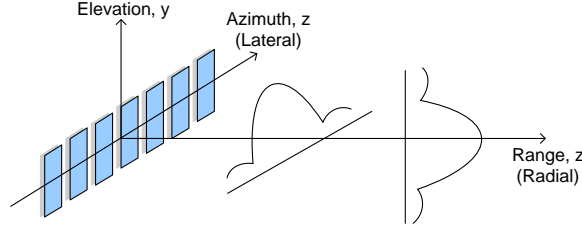


Figure 2.4: Transducer geometry and corresponding directions. The range direction, also called radial direction, is along the beam. The azimuth direction, also called lateral direction, is across the beam. The figure illustrates the profiles in the radial and lateral direction. The blue rectangles are transducer elements. The figure is a modified version of a figure found in [1].

If both the transmit and receive aperture functions are rectangular, the convolution of these two responses gives that the lateral pulse-echo response is a triangular function in k-space. The Fraunhofer approximation states that the ultrasound beam's pressure amplitude can be estimated by taking the 2D Fourier transform of the transducer aperture. The approximation is based on different requirements and assumptions so it only holds for beam patterns in the far field of an unfocused transducer or the focal plane of a focused transducer [1]. This means that by investigating the aperture functions, we can approximately determine the beam profile in the focal plane of a focused transducer. The Fourier transform of a triangular function gives a sinc^2 function. Accordingly, the spatial variations of a pulse-echo response in the focal plane with rectangular aperture correspond to a sinc^2 function in the lateral direction where the sinc function is defined as

$$\text{sinc}\left(\frac{x_{az}}{f_{\#}\lambda}\right) = \frac{\sin\left(\pi\frac{x_{az}}{f_{\#}\lambda}\right)}{\pi\frac{x_{az}}{f_{\#}\lambda}} \quad (2.1)$$

where λ is the wavelength, $f_{\#}$ is the f-number and x_{az} is the azimuth coordinate. The f-number is defined as the focus point divided by the aperture. Fourier transformation of only the transmit or receive aperture gives a sinc function. This is shown in Figure 2.5. In the radial direction the spatial frequencies are usually presented as temporal frequencies.

The beam profile in the elevation direction has in general the same shape as for the azimuth, i.e. lateral, direction apart from some minor changes if the transducer size is different in the azimuth and elevation direction. While the shape of a rectangular aperture corresponds to a sinc^2 function, the shape of a circular aperture is proportional to a jinc^2 function[†].

The beam width is defined as the width of the main lobe. The beam width at the focus point can be used as a measure of the lateral resolution, which is

[†]The jinc function is defined as

$$\text{jinc}(x) = \frac{2J_1(\pi x)}{\pi x} \quad (2.2)$$

where J_1 is the Bessel function of first kind and first order.

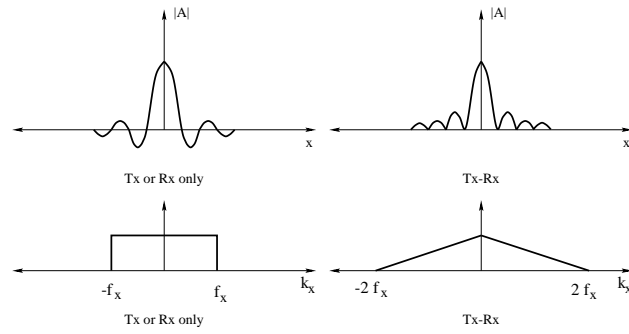


Figure 2.5: Amplitude and k-space responses for a rectangular aperture. The upper left of the figure shows the transmit-only or receive-only amplitude, and the upper right of the figure shows the transmit-receive amplitude. The lower left of the figure shows the transmit-only or receive-only k-space response, and the lower right of the figure shows the transmit-receive k-space response. The figure is found in [1].

explained more in Section 2.8.1. The beam profile can accordingly be used to measure the resolution and also show if the aperture is reduced.

It is also possible to plot the intensity of the beam along the beam direction. The maximum intensity will here be in front of the focus point. This is due to diffractions that arise since the transducer diameter consists of a limited number of wavelengths [16].

2.4 Point Spread Function

The point spread function (PSF) of an imaging system is the response of a point object in the image. It describes how an infinitely small point looks like through an imaging system. An image can be expressed by a convolution between the object field and the PSF,

$$\text{Image} = \text{Object} * \text{PSF} \quad (2.3)$$

This is illustrated in Figure 2.6.

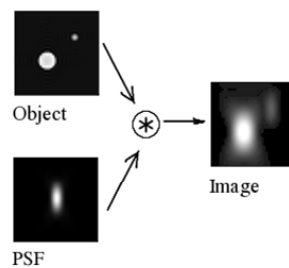


Figure 2.6: An image can be expressed as a convolution between the object and the point spread function. The figure is found in [27].

A point target in a point \vec{r}_0 gives the image $h(\vec{r}, \vec{r}_0)$. The PSF is the impulse response $h(\vec{r}, \vec{r}_0)$ and its Fourier transform is the transfer function of the system, $H(k)$. Eq. 2.3 can now be expressed in the k-space,

$$G(k) = F(k) H(k) \quad (2.4)$$

where $G(k)$ and $F(k)$ are the Fourier transform of the image function and the object, respectively.

Figure 2.7 shows an illustration of the PSF in k-space. The width of the PSF in k-space along k_z is limited by the transmitted pulse. Since the pulse has finite length, the PSF can be seen as a bandpass filter in the radial direction. The size of the PSF in k-space along k_x is limited by the aperture functions. Both the transmit and receive aperture function are rectangular in k-space. As mentioned earlier, the convolution of these aperture functions results in a triangular function and the PSF can be seen as a lowpass filter in the lateral direction. The limited bandwidth of the filter transfer function smears the image and by doing so, defines the spatial resolution of the system.

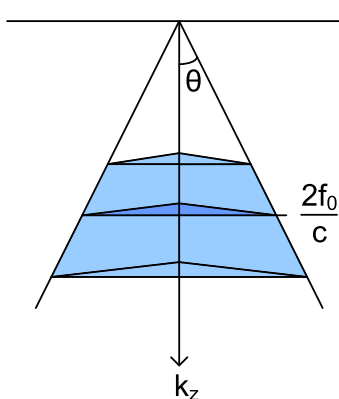


Figure 2.7: The point spread function (PSF) in k-space. The width of the PSF is in the k_z direction limited by the transmit pulse, and in the k_x direction limited by the aperture functions.

The PSF is complex to model accurately because of the interaction of radial and lateral characteristics [28]. When a phantom is used, which is explained in Section 2.7, point targets are being imaged. Since imaging a point target gives the PSF, the PSF will correspond to the spatial resolution of a point target. This resolution is determined by the size of the point target.

2.5 MLA

Standard beamforming consists of generating one scan line when receiving data from one transmit pulse. The receive direction will then coincide with the transmit direction. Multi-line acquisition (MLA), also called parallel beamforming, uses several simultaneous receive beams for every transmit beam [3, 18]. This is illustrated in Figure 2.8. The main lobe of the transmit beam will be broad to include a region that covers the multiple receive beams. When the MLA

technique is used, the number of transmit beams can be reduced and we get the advantage of higher framerate. But increasing the number of MLAs will also mean that the main lobe of the transmit beam must be wider, and this results in smaller transmit aperture. Smaller transmit aperture will next result in reduced resolution. MLA can also give loss in contrast resolution and penetration. It is accordingly not desirable to increase the number of MLAs to as high as possible.

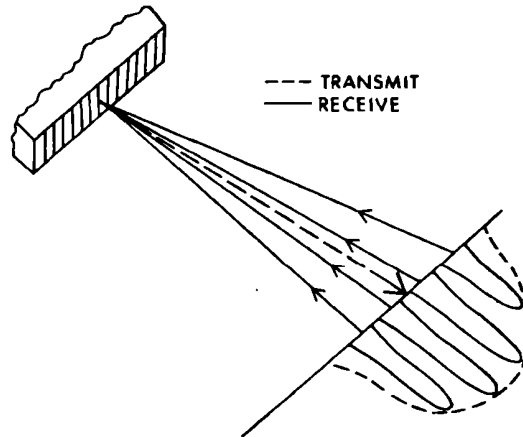


Figure 2.8: Multi-line acquisition (MLA), also called parallel beamforming, uses several simultaneous receive beams for every transmit beam. The main lobe of the transmit beam will be broad to include a region that covers the multiple receive beams. The figure is found in [18].

When MLA is applied, the imaging system becomes spatially variant. Spatial variance is explained in more detail in Section 5.1. The variance introduces artifacts in the image and the most common problem is the block artifact. This artifact occurs as lateral blocks in the image and is due to the misalignment of the transmit and receive beam directions when using MLA. This causes the two-way beam to be pulled towards the transmit beam direction, an effect called warping. The warping is typically strongest at the focal depth, and it leads to gaps between neighboring MLA groups. Misalignment of the beams also causes an effect called skewing. The skewing effect makes the two-way beam profile asymmetrical, and the beam becomes more sensitive on one side than on the other [3].

2.6 Speckle

Ultrasound images have a grainy appearance with bright and dark variations in the image which is called speckle. Closely located point scatterers[†] may be covered by the same ultrasound pulse. The backscattered signals from these scatterers will interfere with each other and introduce a random interference pattern. This pattern is called speckle and is marked in Figure 2.9. The texture

[†]A scatterer is a reflecting object that will scatter a portion of the wave energy in all directions [16].

of the speckle pattern does not correspond to the underlying tissue, and speckle is therefore viewed as noise and has a negative impact on ultrasound imaging [1]. Even so, the speckle pattern is often used to track underlying tissue which is useful in several applications.

The speckle pattern depends on frequency, transducer position, beam width and direction of propagation [9]. If the transducer position and the acquisition parameters are unchanged for several recordings, the images will display the same speckle pattern for every image. By increasing the frequency, the speckle becomes finer grained.

2.7 Phantoms

Ultrasound can be used to visualize many different internal organs as the heart, liver, bladder etc. In this thesis, the focus will be on imaging phantoms. An ultrasound phantom is a container consisting of one or more tissue mimicking materials and different targets. The mimicking material has similar properties as tissue with respect to velocity, scattering and attenuation. The different targets can be point targets, cystic targets, high contrast targets and so on.

When a living organ is scanned, it is not possible to know if structures on the screen come from the targets being imaged or from the scanner itself. By imaging a phantom, the expected image appearance is known and phantoms are often used in quality controls of the scanner.

In this thesis, the phantom CIRS40 has been used [5]. Figure 2.9 shows an image of the phantom where a point target, a cyst and speckle are marked. The point target where the vertical and horizontal point targets intersect is in this thesis called the center point target.

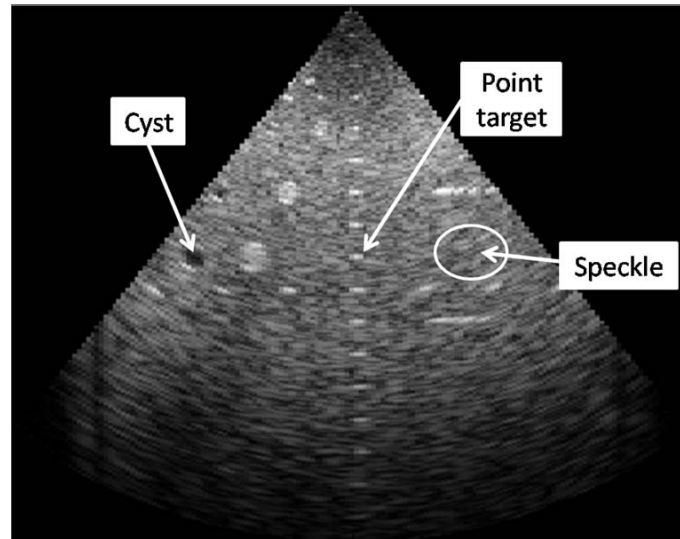


Figure 2.9: Image of phantom CIRS40 with marked point target, cyst and speckle.

2.8 Image Quality

The image quality in ultrasound can be described by two main factors; spatial resolution and contrast resolution [16].

2.8.1 Spatial resolution

Spatial resolution indicates the radial and lateral resolution.

Radial resolution is the closest distance between two objects along the axis of the beam which are displayed as two distinct objects. Objects with closer distance than this resolution will merge together in the image. Radial resolution is also called axial resolution, range resolution and depth resolution. It is expressed as

$$\Delta r = \frac{c \cdot T_p}{2} = \frac{c}{2 \cdot B}, \quad (2.5)$$

where T_p is the pulse length, B is the pulse bandwidth and c is the speed in human tissue (~ 1540 m/s). Eq. 2.5 shows that the resolution is determined by the pulse length, frequency, since $f = \frac{1}{T}$, and the bandwidth of the transducer. It is also dependent of the number of pulse periods. A short pulse gives good radial resolution, but it will also decrease the depth of penetration.

Lateral resolution is the closest distance between two objects transverse to the beam that are displayed as two distinct objects. The resolution is determined by the beam width at the focus point which is defined as

$$\Delta l = k \frac{\lambda \cdot F}{D} = k \cdot \lambda \cdot f_{\#}, \quad (2.6)$$

where F is the focus, D is the aperture and k is a scaling constant. The formula shows that the lateral resolution is improved by increasing the transmit frequency, since $\lambda = \frac{c}{f}$, increasing the aperture and by focusing the beam. The resolution will also be improved by small separation between the beams. The scaling constant is dependent of the shape of the transducer.

While the radial resolution is quite constant with depth, the lateral resolution changes with depth. Both the radial and lateral resolution will influence objects that are smaller than the resolution size. These objects will appear to be at least the resolution size even though the objects are smaller.

The spatial resolution is a valuable parameter for image quality metrics. It is defined in [22] as the radial, or lateral, full-width-at-half-maximum (FWHM)[†], i.e. -6 dB width, of the image of a small object at the focus. When imaging a phantom, the spatial resolution can be determined by the size of the point target.

2.8.2 Contrast resolution

Contrast resolution is the minimum difference in signal strengths from adjacent structures that allows the observer to observe the structures as separate entities [9]. It shows the ability to discriminate a weak target that is close to a strong one. The cyst is a good example of a weak target since it contains a region in the image with no scatterers. The main limitation of contrast resolution

[†]FWHM is given by the distance between points on the curve at which the function reaches half its maximum value.

is acoustic noise generated by the transmitted signal. The noise is caused by the side lobes and multiple reflections of the ultrasound pulse. The contrast resolution is accordingly improved by reducing the side lobe level. Electronic noise will also limit the resolution [16].

The contrast resolution is also called the local dynamic range of the image. Local dynamic range is the ratio between the amplitude of the signal around a cyst to the signal from side lobes and reverberations inside the cyst. The local dynamic range is at the most approximately 50-60 dB. It must not be misinterpreted with total dynamic range which is the ratio of the strongest signal from close targets to the weakest signal from very deep targets [16].

Different methods and names are used in the literature when contrast resolution is determined. The phantom used in this thesis includes both cystic targets and high contrast targets. Cystic targets are liquid filled and anechoic, while high (and low) contrast targets are typically 3 to 15 dB above (and below) the background level. These are evaluated differently in the literature in terms of contrast resolution. For a cystic target, the tissue-to-clutter ratio (TCR) is in [21] defined as

$$\text{TCR} = 20 \log_{10} \frac{\langle \mu_B \rangle}{\langle \mu_L \rangle} \quad (2.7)$$

where $\langle \rangle$ means averaging over multiple scans, and μ_B and μ_L are mean gray level of background and cyst, respectively.

In [21], only low and high contrast targets, and not anechoic targets like cysts, are assigned with a contrast resolution. It is convincible to evaluate the TCR as a contrast resolution parameter for anechoic targets. This agrees with other literature that describes contrast resolution for anechoic targets as the difference between average brightness level of the cyst's centre and the background [24]. It also resembles the definition of local dynamic range by [16].

In [8] by Gibson et al., the anechoic objects are determined by calculation of the correlation coefficient between the detected target and an ideal target, where a matched filter is used. At the same time, Gibson et al. use almost the same formula as the above equation, Eq. 2.7, when the resolution for low and high contrast targets is determined.

For high contrast targets, contrast-to-noise ratio (CNR) is defined in [21] as

$$\text{CNR} = \frac{|\mu_B - \mu_L|}{\sqrt{(\sigma_B + \sigma_L)/2}} \quad (2.8)$$

where σ_B and σ_L are variance of gray levels within background and lesion, respectively.

As it can be seen, all methods include many of the same parameters, but with some small changes in the calculations. It seems like there is no unambiguous definition of the contrast resolution, but the main focus consists of comparing the values inside and outside of the target.

2.8.3 Other image quality parameters

Other parameters related to image quality are among other things sharpness, artifacts, geometric distortion, noise and temporal resolution [9].

Sharpness describes the ability of the scanner to reproduce tissue boundaries [9]. It is closely related to spatial resolution and is seldom evaluated on its own. The sharpness of the tissue boundaries is associated with acutance, which is how quickly the transition at an edge is. High acutance is difficult to obtain in ultrasound images, but it can still be a useful parameter when determining the image quality.

An artifact is a structure in the image that does not provide a true representation of the scanned object. Artifacts can be objects in the image that are not actually present, structures that should be represented in the image but are missing, and structures whose locations in the image are wrongly registered [9]. An image artifact is sometimes caused by improper use of the scanner, but mostly it is a consequence of properties in the body. Most artifacts degrade the image quality and can lead to misdiagnosis, but the artifacts are at the same time inherent in the imaging process and cannot be totally eliminated.

The scanned structures should accurately correspond to the structures displayed on the screen. If this is not the case, we have geometric distortion. It is caused by variations in wave velocity and structures will be wrongly placed in the displayed image.

Noise is the random variation in signal amplitude measurements of detected echoes and causes brightness fluctuations in the ultrasound image [9]. Noise can be divided into electronic and acoustic noise. The electronic noise originates primarily from amplifiers and cross-coupling of cables, while acoustic noise may result from side lobes and grating lobes, and from false reflections and refractions [19].

Temporal resolution is a measure of the fastest detectable moving object and refers to the ability to accurately visualize moving objects. Temporal resolution is limited by the frame rate, and an increase of the frame rate will result in better temporal resolution. It will at the same time either decrease the lateral resolution or the imaging field.

Chapter 3

Related Theory

In addition to ultrasound theory, it can be useful for the reader to have some knowledge about the theory and methods related to the two main topics presented in this thesis. Correlation is heavily used when evaluating the spatial variance and a brief introduction to correlation coefficient and also to template matching is first presented. Next, spectral analysis is presented which is related to the power spectrum calculations in the ProbeContact algorithm.

3.1 Correlation

Correlation indicates the degree of linear relation between two signals. For 1 dimension, the unbiased correlation function can be expressed as

$$R_{xy}[l] = \langle x[n] y^*[n-l] \rangle \quad (3.1)$$

$$= \frac{1}{N} \sum_{n=0}^{N-1} x[n] y^*[n-l] \quad (3.2)$$

where $\langle \rangle$ denotes the mean of the variable and $*$ denotes complex conjugate. With lag 0, the above equation becomes

$$R_{xy}[0] = \frac{1}{N} \sum_{n=0}^{N-1} x[n] y^*[n] \quad (3.3)$$

When the term correlation is used, it often refers to cross correlation which means that two distinct functions are evaluated. When $x[n]$ and $y[n]$ are identical, the formula expresses the autocorrelation.

The correlation function is sensitive to changes in the amplitude, and it is common to defeat this disadvantage by using the normalized correlation coefficient. The normalized correlation coefficient is given by

$$r = \frac{1}{N} \sum_{n=0}^{N-1} \left(\frac{x[n] - \bar{x}}{s_x} \right) \left(\frac{y[n] - \bar{y}}{s_y} \right)^* \quad (3.4)$$

where \bar{x} denotes the mean and s_x denotes the standard deviation of x^\dagger [13].

$$^\dagger s_x = \sqrt{\frac{1}{N} \sum_{n=0}^{N-1} (x[n] - \bar{x})^2}$$

By comparing this equation with Eq. 3.3, it can be seen that $x[n]$ is exchanged with $\frac{x[n]-\bar{x}}{s_x}$ and the corresponding with $y[n]$. This is the normalization, also called standardization, of the signal. The normalization removes the scale dependence and the coefficient will be in the range -1 to 1. If $r = \pm 1$, there is a perfect linear relationship between the two functions. The correlation coefficient is also known as the Pearson's correlation or product-moment coefficient of correlation.

The correlation coefficient can be rewritten to

$$r = \frac{1}{N} \sum_{n=0}^{N-1} \left(\frac{x[n] - \bar{x}}{s_x} \right) \left(\frac{y^*[n] - \bar{y}^*}{s_y^*} \right) \quad (3.5)$$

$$= \frac{1}{N} \sum_{n=0}^{N-1} \frac{(x[n] - \bar{x})}{\sqrt{\frac{1}{N} \sum_{n=0}^{N-1} (x[n] - \bar{x})^2}} \frac{(y^*[n] - \bar{y}^*)}{\left(\sqrt{\frac{1}{N} \sum_{n=0}^{N-1} (y[n] - \bar{y})^2} \right)^*} \quad (3.6)$$

$$= \frac{1}{N} \frac{\sum_{n=0}^{N-1} (x[n] - \bar{x}) (y^*[n] - \bar{y}^*)}{\sqrt{\frac{1}{N^2} \sum_{n=0}^{N-1} (x[n] - \bar{x})^2 \sum_{n=0}^{N-1} (y^*[n] - \bar{y}^*)^2}} \quad (3.7)$$

$$= \frac{\sum_{n=0}^{N-1} (x[n] - \bar{x}) (y^*[n] - \bar{y}^*)}{\sqrt{\sum_{n=0}^{N-1} (x[n] - \bar{x})^2 \sum_{n=0}^{N-1} (y^*[n] - \bar{y}^*)^2}} \quad (3.8)$$

For 2 dimension, the correlation with lag 0 becomes

$$R_{xy}[0] = \frac{1}{MN} \sum_{n=0}^{N-1} \sum_{m=0}^{M-1} x[n, m] y^*[n, m] \quad (3.9)$$

and the normalized correlation coefficient becomes

$$r = \frac{\sum_{n=0}^{N-1} \sum_{m=0}^{M-1} (x[n, m] - \bar{x}) (y^*[n, m] - \bar{y}^*)}{\sqrt{\sum_{n=0}^{N-1} \sum_{m=0}^{M-1} (x[n, m] - \bar{x})^2 \sum_{n=0}^{N-1} \sum_{m=0}^{M-1} (y^*[n, m] - \bar{y}^*)^2}} \quad (3.10)$$

If the dimensions of the image are large, the calculations can tend to be slow and inefficient. This can be solved by performing the calculations in the frequency domain by use of Fast Fourier Transform (FFT).

3.1.1 Template matching

Template matching is a technique used in classifying objects and consists of finding small parts of an image which match a template image. The template image is shifted to every location in the larger source image and for each position it is calculated how well the template matches the source image. Correlation is often used for the matching process, and the cross correlation will

be maximum at the location where the template finds a correspondence in the source image. An object can then be classified by searching for peaks in the cross correlation function. Template matching for a pattern of gray-scale values is shown in Figure 3.1

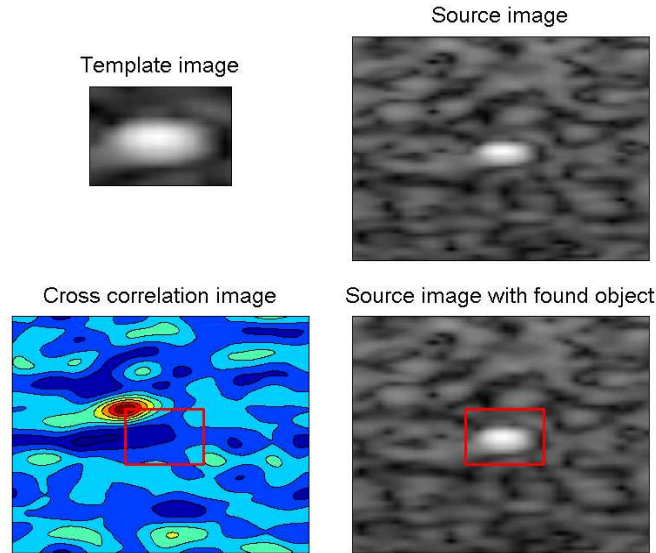


Figure 3.1: Template matching of a pattern of gray-scale values. The template image is applied to every possible position in the source image. The position of the peak in the cross correlation image represents the location in the source image where the upper left corner of the template image matches best with the source image. The red square marks the location of the best match.

3.2 Spectral Analysis

The process of obtaining a representation of the frequency components in a signal using basic mathematical tools is known as spectral analysis [14]. This applies when the signal is infinite and an exact mathematical description is possible. In practical problems, we attempt to extract the relevant information in the signal, and the spectrum can only be estimated.

The different methods when spectral analysis is performed, can be divided into two categories: classical methods and modern methods. Classical methods are based on the Fourier transform and modern methods are based on the estimation of model parameters [17]. Every spectral analysis method has its strengths and weaknesses related to specific spectral features. Two important spectral features are the overall shape of the spectrum and local features of the spectrum. Since methods that provide good overall estimates, give poor local estimates, and vice versa, the methods must be chosen by evaluating which features that are the most important for the given situation.

3.2.1 Power spectrum

A power spectrum shows how the power of a periodic signal is distributed among the various frequency components and can be expressed as

$$G(\omega) = |X(\omega)|^2 \quad (3.11)$$

where $X(\omega)$ is the Fourier transform of the signal $x(t)$. This way of calculating the power spectrum is called the direct method. A second approach is the indirect method, and the power spectrum is calculated by first computing the autocorrelation from $x(t)$ and then computing the Fourier transform of the autocorrelation.

Eq. 3.11 applies if the signal has infinite length. But, as already mentioned, this is not the case in practice. The power spectrum must then be calculated from a limited set of samples in the signal, and it is common to average the signal when the power spectrum is calculated. This is referred to as an average periodogram. Averaging is usually achieved by dividing the waveform into a number of segments, possibly overlapping, and evaluating the Fourier transform on each of these segments. The power spectrum is then an average of the Fourier transforms from the various segments [15].

3.2.1.1 Windowing

When a Fourier transform is computed from a non-periodic data segment, the resulting spectrum suffers from leakage. When leakage occurs the signal energy smears out, and the solution to the problem is to apply an appropriate window function. A window function is exactly zero at the edges and with some special form in between. It then forces the signal to start and end at zero to mimic a periodic signal.

By applying a rectangular window function, the spectrum is widened (main-lobe) and additional peaks are generated (sidelobes). This is also present for other windows, and common window types like the Hamming and triangular window, reduce the sidelobes with the result of wider mainlobe.

When multiplying the signal by a window function, the signal power is reduced because of the suppressed ends. The signal must then be scaled by a coherent power gain to retain its original power and amplitude. The coherent power gain is the square of the sum of the elements in the window function. It is usually normalized by dividing by the number of terms N , so that if a rectangular window function is used, the coherent power gain would be normalised to 1 [15].

Part II

Methods and Implementation

Chapter 4

Tools

This chapter presents the tools used in this thesis. All implementations and simulations are done in MATLAB version 7.8.0 R2009a.

4.1 Scanner Setup

A GE Vivid 7 Ultrasound scanner was used when recording the phantom images. Table 4.1 summarizes the used settings on the ultrasound scanner. A GE M3S phased array probe was used. The demodulation frequency and bandwidth were fixed. It has been used fundamental imaging mode and dynamic focus on receive.

Table 4.1: Table of scanner settings

<i>Parameter</i>	<i>Value</i>
Frequency	2.5 MHz
Pulse length	0.6 μs
Aperture	22 mm
Focus	90 mm
Depth	16 cm
Sector width	35°

4.2 GcMat

GcMat (Graphic Component for MATLAB) is a tool for displaying and manipulating ultrasound data from the scanner in MATLAB. The system is developed by the Department of Circulation and Medical Imaging (ISB) at NTNU in collaboration with GE Vingmed Ultrasound.

GcMat has been used in this thesis to retrieve recorded images from the ultrasound scanner so they could be used in the spatial variance algorithm, explained in Chapter 5, and in the ProbeContact algorithm, explained in Chapter 6. GcMat version 7.0.511 has been used.

4.3 Field II

Field II is a program that simulates ultrasound fields and images and is interfaced with MATLAB [10]. The program assumes that the pressure field has linear propagation and is able to calculate the pulsed and continuous pressure field for different transducers. The transmitted field is calculated by convolution of the excitation, the transmit transducer impulse response and the transmit spatial impulse response.

Field II is an extremely useful simulation tool, but it should be noted that the system assumes linear propagation of ultrasound waves, which is not the truth. In addition, the accuracy of the calculations of the field will increase with increasing distance from the transducer. This is because Field II uses a far field approximation, and it will result in degraded image quality in the near field.

Field II has been used in this thesis to simulate the CIRS Model 40 phantom [5]. All variables in Field II were assigned exactly as the settings on the ultrasound scanner, so that the simulated images would be equivalent to the images recorded on the scanner. GE's acoustical model has been used to reveal some of the parameters, and the simulation uses IQ-demodulated data.

4.4 Existing Image Analysis System

The basis for this thesis is an image analysis system that was developed during the project assignment [20]. The system finds point targets and cysts in the image and describes their characteristics related to image quality. To be able to perform the image analysis, the image must be recorded with five frames and make sure of placing five point targets within these frames. This is shown in Figure 4.1. The system will then search inside the frames and find the point targets. Based on the location of the point targets in the frames, other point targets and cysts can also be found. The system gives information about profiles, resolution, contrast parameters and gain balance in the image.

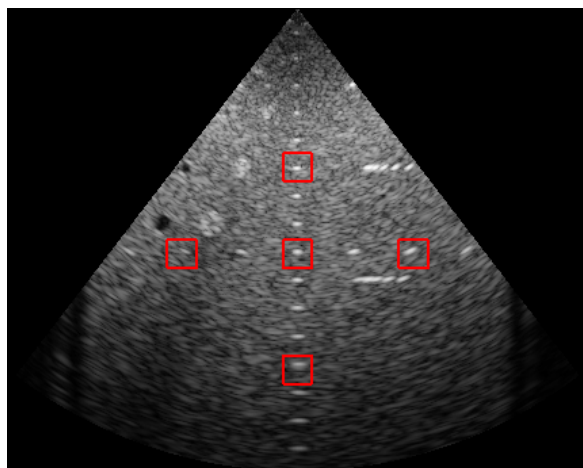


Figure 4.1: Recorded image with five frames in existing image analysis system. Point targets must be placed within these red frames.

Chapter 5

Spatial Variance

Two main topics have been investigated in this thesis. One of them was spatial variance and will be presented in this chapter. The chapter is divided into background information, implementation and methods used to evaluate the spatial variance.

5.1 Background

If a system is spatially invariant, a structure in the image will appear the same, regardless of where in the image it is placed [2]. Spatial invariance is also commonly called shift invariance. In a spatially invariant imaging system, the PSF will be identical in all parts of the image, and spatial invariance is clearly a desirable characteristic of an imaging system. For an imaging system to be spatially invariant, the following must be satisfied [3]:

1. The two-way response of each imaging beam must be equal in shape
2. The two-way response of each imaging beam must be equally spaced
3. The distance between each imaging beam must satisfy the Nyquist sampling theorem

If the beams have different shape, that is item 1 is not fulfilled, geometrical distortion will be introduced. Item 3 is satisfied if the spacing of the beams are no more than the Nyquist sampling theorem for ultrasound, that is $f_{\#}\lambda$. This is also called the Rayleigh criterion. If item 3 is not satisfied, we will have undersampling and information will be lost. Both of these sources for spatial variance can be considerably reduced by thorough system design. Item 2 is normally satisfied when we have the common situation with one receive beam for each transmit beam.

Complete spatial invariance is only valid for ideal systems, but ultrasound imaging systems are often approximated to be spatially invariant. This is accepted by looking at the system as *locally* spatially invariant. Even though a PSF is spatially variant, it can be approximated to be locally spatially invariant because the spatial variability of the PSF, due to attenuation and aberration, is slowly varying [4].

Spatial variance is an important image quality parameter. As the spatial variance always will be present, it can be useful to measure this parameter since high variance can lead to misleading interpretations.

5.2 Implementation

To measure the spatial variance of a point target, the system calculates the cross correlation of the same region in different frames. The probe is tilted to the side for increasing frames, and the point target moves a small distance for every frame. The correlation coefficient between two frames gives a good indication of the spatial variance since it measures how similar the two point targets are. If the point target changes its shape, the correlation will decrease. This will also imply that the point target is spatially variant.

More precisely, the evaluation of spatial variance starts with searching for the frame which consists of a specific point target that has the smallest width compared to the same point target for other frames. This frame will be the reference frame, and it is chosen so that the point target in the other frames will be compared to a point target with good resolution, that is a point target that is as close as possible to a transmit beam. This is an important step when the beam density is low or when using MLA. The point target in the reference frame is found by use of the existing image analysis system mentioned in Section 4.4. Based on the center point of the point target, a region of interest (ROI), containing the point target, is defined.

In addition, a larger ROI is created for each frame which is certain to contain the corresponding point target. This moving point target is now found by use of template matching between the two ROIs. For every frame, the process of first defining a large ROI in the current frame and then matching this with the ROI from the reference frame is executed. The matching process will find the right point targets, and the large ROIs are adjusted to only contain the found point targets. For every frame, the current ROI is compared with the ROI from the reference frame, and the normalized correlation coefficient is calculated from Eq. 3.10.

The algorithm is also implemented with calculations of the correlation coefficient for different ROIs which only contain speckle. The speckle ROIs are for each frame defined as a region above the center point of the point target for the current frame. Next, the correlation coefficient is determined by comparing the different ROIs with the speckle ROI from the reference frame in the same manner as before.

For each frame, the distance between the present point target and the point target from the reference frame is calculated. This is used in the correlation coefficient plots. The distance is calculated by looking at six different point targets in each frame. The angles between the point targets in the reference frame and the corresponding point targets in the other frames are measured, and by averaging over the six angles for each frame, the distances between the frames are determined. By using more than one point target when the angle between two frames is measured, the distance calculation gets more robust.

The algorithm is independent of the tilting direction since the spatial variance should be equal regardless of which way the probe is tilted.

5.3 Methods

The implemented spatial variance algorithm has been tested for five different cases. The first one was testing the algorithm on scanned and simulated images with four different beam densities. The images consisted of 81, 48, 24 and 19 beams. Other system properties are listed in Table 4.1.

As discussed in Section 2.2, the data after logarithmic calculations is called beamspace tissue data while the data after IQ-demodulation is called IQ-data. The calculations of spatial variance use beamspace tissue data. But the spatial variance was also tested when it was calculated from IQ-data. This was done for a simulated image with 48 and with 24 beams.

In addition, the spatial variance has been studied for ROIs which only consist of speckle pattern. It has both been tested on recorded and simulated images with 48 and 24 beams. Also, spatial variance of the speckle pattern calculated from IQ-data has been tested.

The above cases use the same point target, the center point target, in the calculations. The spatial variance was studied for different point targets located at different depths in the image; one point target from the upper part of the image, one point target from the center and one point target from the lower part of the image. The three point targets did then vary in depth, but were aligned above each other. It was tested for scanned and simulated images with 48 and 24 beams.

The last case tested was spatial variance for scanned and simulated images with 2 and 4 MLA. The images contained 80 receive beams.

When the images on the scanner were recorded, the probe was manually tilted. The number of frames did then vary. Manual tilting resulted in some irregularities since it is very difficult to tilt the probe exactly the same angle for each frame and to retain in the same 2D plane for the entire recording.

To be able to give a thorough analysis of the spatial variance and to test all the cases, six different images were recorded on the scanner; four images with different beam densities and two images with different MLAs. The four images with different beam densities were obviously used to calculate the spatial variance for different beam densities, but also when the spatial variance was calculated from IQ-data and when spatial variance was determined for speckle pattern and various point targets. The two images with different MLAs were naturally used when the spatial variance was tested for different MLAs.

Because of the difficulty of achieving solid results when manually tilting the probe and as a basis for comparison, the corresponding scenarios were simulated in Field II. The first frame was simulated with no tilting. For the other frames, a rotation matrix with increasing rotation angle θ was used. As the system is 3 dimensional and it was desirable to tilt the point target in the lateral direction, the rotation matrix is defined as [6]:

$$R_{\theta} = \begin{bmatrix} \cos(\theta) & 0 & -\sin(\theta) \\ 0 & 1 & 0 \\ \sin(\theta) & 0 & \cos(\theta) \end{bmatrix} \quad (5.1)$$

The simulated images were tilted from 0 to 6 degrees divided among 99 frames. Six different images were simulated which correspond to the six recorded images.

Chapter 6

ProbeContact

This chapter presents the implementation and methods for the other main topic in this thesis; different power spectra, and their respective mean frequency and bandwidth, in the ProbeContact algorithm. But first, the algorithm will be briefly explained.

6.1 Background

ProbeContact is an algorithm developed at the Department of Circulation and Medical imaging (ISB), and it provides the user with real time feedback of the acoustic contact between the probe and the patient's skin [12]. If the contact is poor, the complete aperture of the probe will not be used and this will result in degraded image quality. The algorithm is an important method related to objective image quality metrics since it is able to give the user feedback on the probe contact which is connected to the quality of the image.

The method estimates and visualizes the lateral power spectrum and uses this to give a good indication of the acoustical contact. The spectrum is calculated by first averaging the radial samples close to the focus and then use a discrete Fourier transform (DFT) over the lateral beams. The method is based on the Fraunhofer approximation. This approximation, also discussed in Section 2.3, states that the lateral spectrum close to focus is bandlimited in k-space by the convolution of the transmit and receive aperture functions. This leads to that the shape of the lateral power spectrum will change correspondingly with change in the effective imaging aperture.

6.2 Implementation and Methods

The ProbeContact algorithm has been incorporated in the image analysis system. In addition, different power spectrum calculations related to ProbeContact and their mean frequency and bandwidth have been evaluated.

6.2.1 Lateral power spectra

The ProbeContact algorithm uses today the simplification of first averaging the radial samples, and then calculating the spectrum by use of the Welch method that utilizes the Fourier transform. It was originally done this way to save

computation time. This thesis wanted to evaluate the impact of switching the order of averaging and the Fourier transform. The following cases have been studied:

1. Averaging to 1 dimension, followed by the Welch method
2. Averaging to 1 dimension, followed by $|\text{1D DFT}|^2$
3. $|\text{1D DFT}|^2$, followed by averaging to 1 dimension
4. $|\text{2D DFT}|^2$, followed by averaging to 1 dimension

where 1D and 2D stands for first and second dimension, and DFT stands for Discrete Fourier Transform.

The different cases are illustrated in Figure 6.1. The 2D power spectrum is denoted as $G(k_x, k_z)$ and the lateral power spectrum as $G(k_x)$. Table A.1 given in Appendix A.1 summarizes the mathematical equations used in the cases. The Welch method is a nonparametric[†] method which divides the signal into overlapping data segments, calculates the periodograms by performing Fourier transform and then averaging the result [14]. The method reduces the noise in the spectrum, but at the expense of few details of the local features. Case 1 and case 2 are then very similar, except for the reduced noise in case 1. The ProbeContact algorithm uses today case 1.

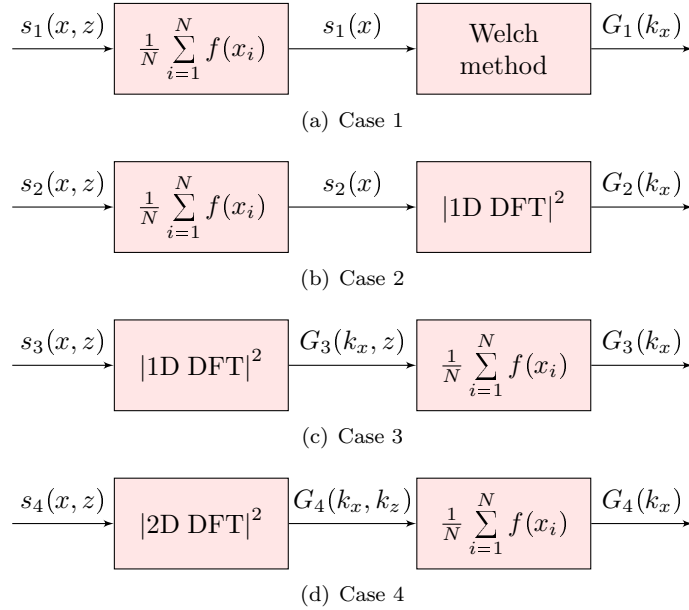


Figure 6.1: The four different cases that have been studied related to the ProbeContact algorithm. $s(x, z)$ is a region in the image and $G(k_x)$ is the 1 dimensional power spectrum in the lateral direction.

[†]No assumption made about how the data were generated

An often used assumption is to neglect taking the absolute value and square of the variables after Fourier transformation is performed. This simplifies the calculations, and without $|\cdot|^2$, case 2 and 3 give the same result. This is derived in Appendix A.2.

But without this simplification, case 2 and case 3 have the relation

$$G_2(k_x) \leq \frac{1}{N'} G_3(k_x) + \frac{2}{(N')^2} |\alpha| \quad (6.1)$$

where N' is the number of elements used when calculating the average, $G_2(k_x)$ and $G_3(k_x)$ are the power spectra for case 2 and 3, respectively and

$$\alpha = \sum_{i=1}^{N'-1} \sum_{l=i+1}^{N'} S(k_x, z_i) S(k_x, z_l)$$

where $S(k_x, z) = \mathcal{F}_x\{s(x, z)\}$. The calculations are given in Appendix A.3. The second term on the right side of Eq. 6.1 cannot be negative, and it is expected that the lateral power spectrum for case 3 will overall have a higher power than for case 2. Since case 2 and 3 did not give the same spectrum, it is clear that case 4 also is different from case 2.

Next, a comparison of case 3 and 4 was attained. Appendix A.4 derive that the relation between the lateral power spectrum for case 3 and 4 is

$$G_4(k_x) = N' G_3(k_x) \quad (6.2)$$

Appendix A.4 shows also that if the normalized Fourier transform has been used, the relation between case 3 and 4 is

$$\hat{G}_4(k_x) = \hat{G}_3(k_x) \quad (6.3)$$

Each case has been evaluated for the same image in the ProbeContact algorithm and the different spectra have been compared with the mathematical results.

6.2.2 Mean frequency and bandwidth

It was desirable to quantify the contact of the probe. Both mean frequency and bandwidth are good spectral parameters for doing so. When the acoustic contact on one or both sides of the probe are poor, the lateral bandwidth will be reduced and the location of the mean frequency relative to zero frequency is shifted. The mean frequency is also used in the calculations of the effective aperture parameter displayed in percent when generating the ProbeContact algorithm.

Mean frequency and bandwidth were calculated as the first and second order central moments of the power spectrum. By assigning the lateral power spectrum as $G(\omega)$, the mean frequency $\bar{\omega}$ is expressed as

$$\bar{\omega} = \frac{\int_{-\infty}^{\infty} \omega G(\omega) d\omega}{\int_{-\infty}^{\infty} G(\omega) d\omega} \quad (6.4)$$

and the bandwidth B as

$$B^2 = \frac{\int_{-\infty}^{\infty} (\omega - \bar{\omega})^2 G(\omega) d\omega}{\int_{-\infty}^{\infty} G(\omega) d\omega} \quad (6.5)$$

The mean frequency and bandwidth have been calculated for all frames and compared for the different cases.

Part III

Results and Discussion

Chapter 7

Results

This chapter presents the results from the evaluation of spatial variance and of different power spectra in ProbeContact. A simple graphical user interface (GUI) has been made to make it easy to test the different scenarios. This system combines the new methods evaluated in this thesis with the image analysis system from the project assignment. More information can be found in Appendix B.

7.1 Spatial Variance

Spatial variance has been tested for a variety of properties. The correlation coefficient is calculated for the different cases and viewed as a measure of spatial variance. If the correlation coefficient is 1, the compared regions are spatially invariant. But if the correlation coefficient decreases from 1, the spatial variance will increase.

First, the results from calculating the correlation coefficient for the four different beam densities will be presented, followed by results of the correlation coefficient for the IQ-data, for the speckle pattern, for the different point targets and for MLAs. Most parts will both present the results from the recordings on the scanner and from the simulations in Field II.

7.1.1 Different beam densities

The correlation coefficient from recorded images on the scanner with a beam density of 81, 48, 24 and 19 beams, are shown in Figure 7.1. The figure shows how the correlation coefficient changes with increasing distance from the reference frame. The distances are given in degrees. Figure 7.2 shows the correlation coefficient where the same beam densities are used, but the images are simulated. The distances between the point target in the different frames are in the figure calculated in the same manner as for the scanner, and as explained in Section 5.2. Figure 7.3 also shows the correlation coefficient for the simulated images, but the distances are now calculated by knowing that the point target moves exactly the same distance for each frame. The simulation images are tilted from 0 to 6 degrees divided on 99 frames. The lateral profiles for a simulated image with 81 and with 19 beams, are shown in Figure 7.4. Each blue line represents the lateral profile of the point target for a given frame, and

the figure shows how the lateral profiles evolve for successive beams. Table 7.1 summarizes the distance between transmit beams at the focus point for different beam densities. It also shows the calculated Nyquist sampling limit.

7.1.2 IQ-data

The correlation coefficients calculated from beamspace tissue data and from IQ-data, are shown in Figure 7.5(a) and 7.5(b) respectively. The image is simulated and has a beam density of 48 beams. Figure 7.6(a) and 7.6(b) show the correlation coefficient for the same settings except for a change in the beam density to 24 beams.

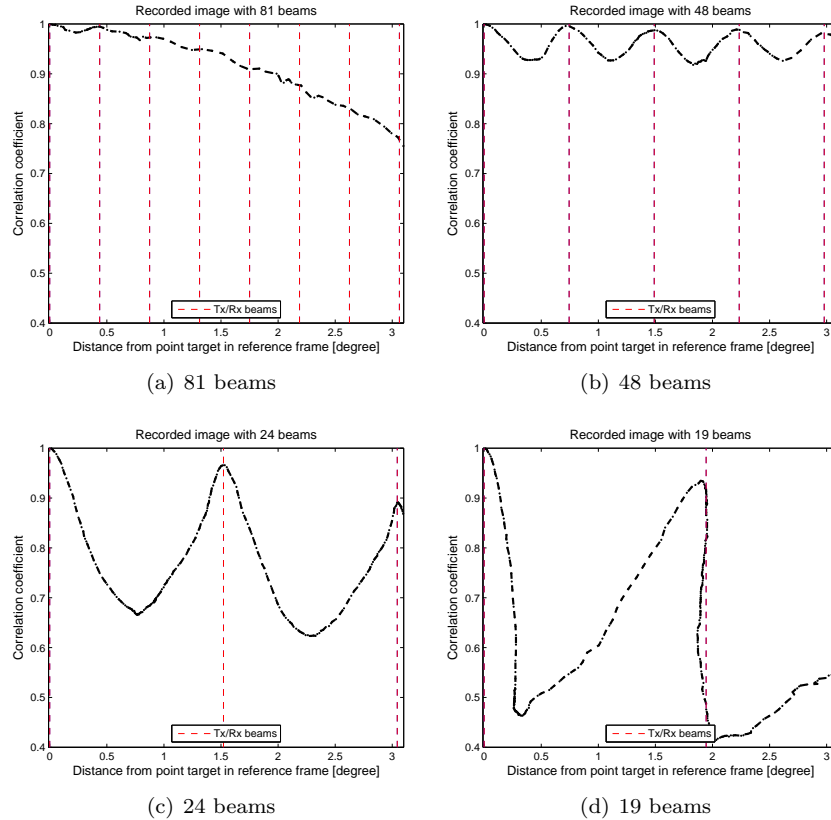


Figure 7.1: Correlation coefficient for the recorded images, with 81, 48, 24 and 19 beams, with increasing distance from the reference frame. The correlation coefficient is determined by comparing a ROI, containing a point target, from a reference frame with the corresponding ROIs from the other frames. Tx/Rx beams stands for transmit/receive beams and illustrates where the beams are located related to the distance from the point target in the reference frame.

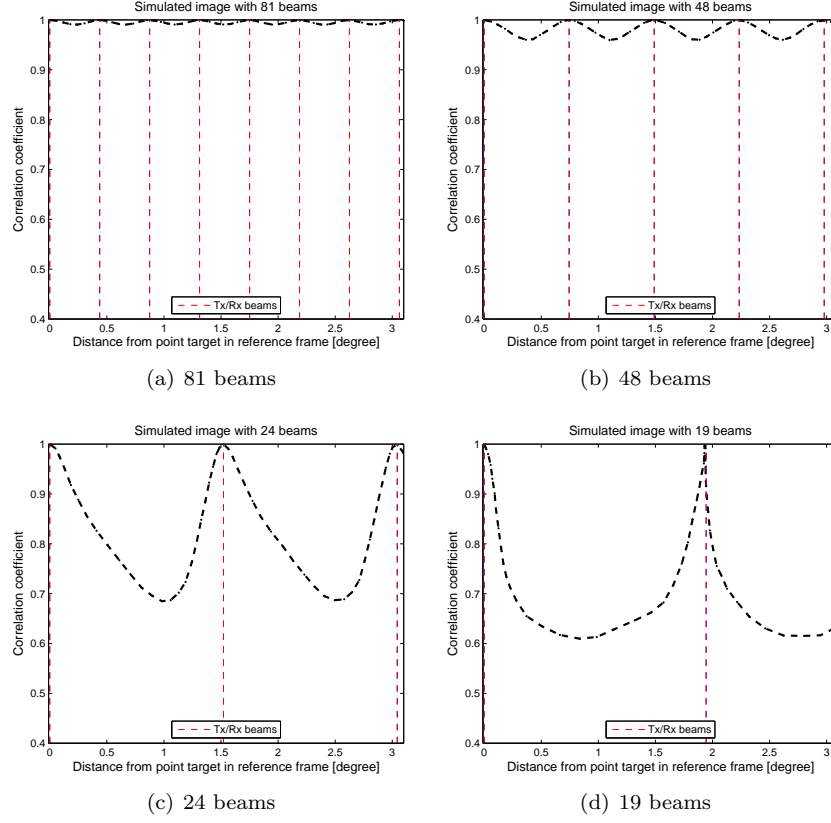


Figure 7.2: Correlation coefficient for the simulated images, with 81, 48, 24 and 19 beams, with increasing distance from the reference frame. Further explanation of the behavior of the figure is as in Figure 7.1.

Table 7.1: Distance between transmit beams at the focus point for different beam densities together with the Nyquist sampling limit.

<i>No. of beams</i>	<i>Distance [mm]</i>
81	0.678
48	1.145
40 (2 MLA)	1.374
24	2.291
20 (4 MLA)	2.749
19	2.894
Nyquist	2.520

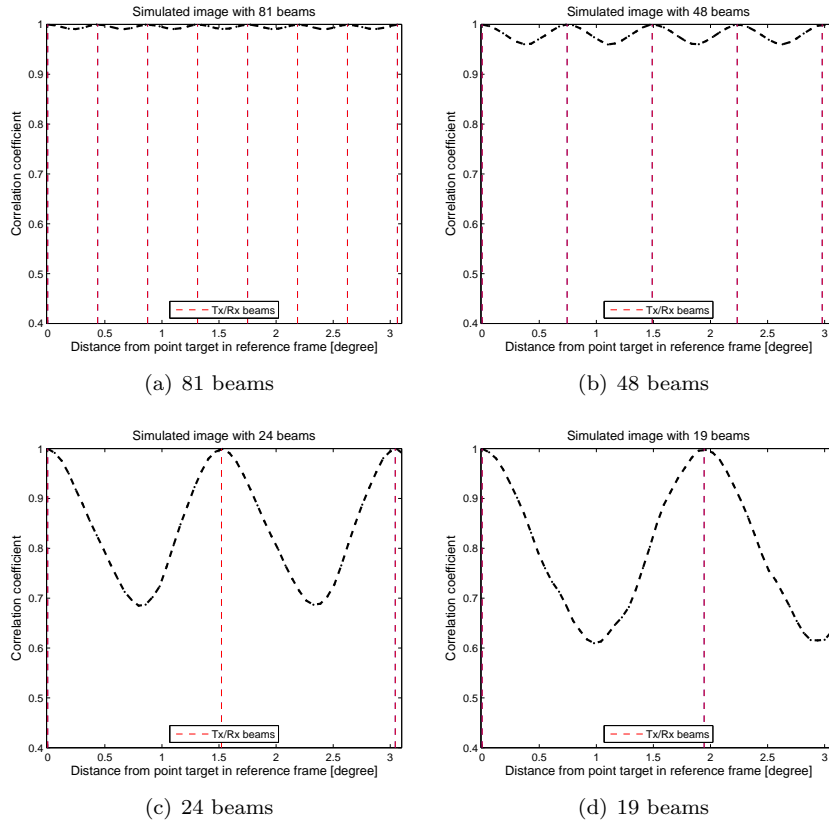


Figure 7.3: Correlation coefficient for the simulated images, with 81, 48, 24 and 19 beams, with increasing distance from the reference frame. The distance is measured by applying that the point target moves an equal distance for each frame. Further explanation of the behavior of the figure is as in Figure 7.1.

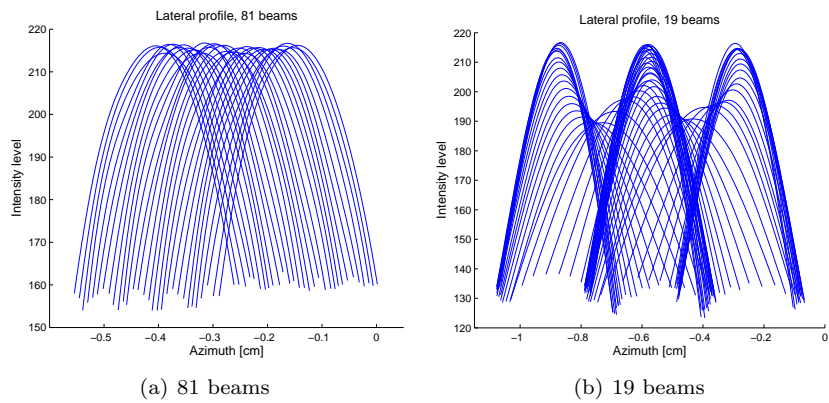


Figure 7.4: Lateral profiles for the simulated images with 81 and 19 beams. Each blue line represents the lateral profile of the point target for a given frame, and the figure shows how the lateral profiles evolve for successive beams.

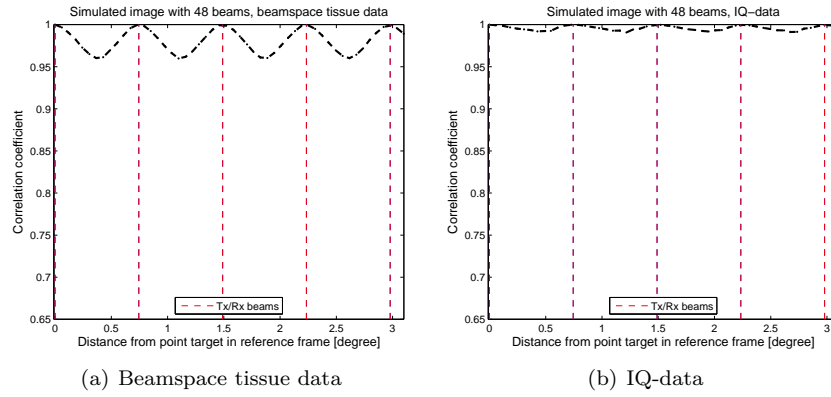


Figure 7.5: Correlation coefficient calculated from beamspace tissue data and from IQ-data for a simulated image with 48 beams. IQ-data represents the data after IQ demodulation, while beamspace tissue data refers to the data after logarithmic compression. Further explanation of the behavior of the figure is as in Figure 7.1.

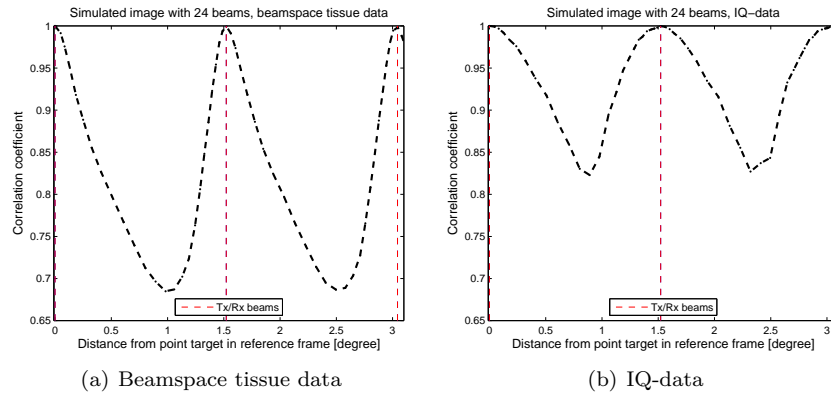


Figure 7.6: Correlation coefficient calculated from beamspace tissue data and from IQ-data for a simulated image with 24 beams. IQ-data represents the data after IQ demodulation, while beamspace tissue data refers to the data after logarithmic compression. Further explanation of the behavior of the figure is as in Figure 7.1.

7.1.3 Speckle pattern

Figure 7.7(a) shows the correlation coefficient calculated from a ROI consisting of a point target (upper part) and the correlation coefficient calculated from a ROI only consisting of speckle (lower part). The image is recorded on the scanner and has a beam density of 48 beams. Figure 7.7(b) shows also the correlation coefficient for a point target ROI and a speckle ROI, but this image is recorded with 24 beams. Figure 7.8 shows the correlation coefficient for the same calculations with different ROIs and the same beam densities, but the images are now simulated. Figure 7.9 shows the correlation coefficient for the same settings as Figure 7.8, but the coefficient is calculated from IQ-data.

7.1.4 Various point targets

Figure 7.10 shows the correlation coefficient for three point targets in a recorded image with 48 and 24 beams, while Figure 7.11 shows the corresponding results for the simulated images. The distances from the reference frame are for both figures shown in millimeters since the distance in degrees varies for the three point targets.

7.1.5 MLA

Figure 7.12 shows the correlation coefficient for a scanned image with 2 MLA and with 4 MLA. The corresponding simulated images are shown in Figure 7.13. Figure 7.14 shows also the results from the simulated images, but the distance axis is again calculated by knowing that the point target moves exactly the same for each frame. Figure 7.15 shows two lateral profiles from the scanned image and from the simulated image with 4 MLA. Every profile from all frames have been compared, and the upper part of Figure 7.15(a) and 7.15(b) displays

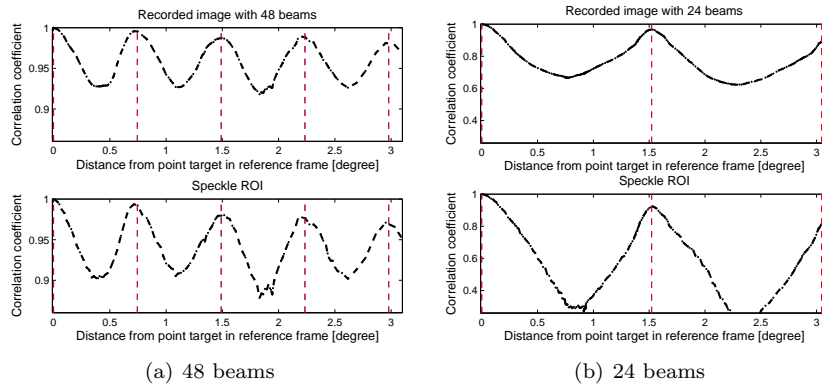


Figure 7.7: Correlation coefficient for the recorded images calculated by point target ROI (upper part) and speckle ROI (lower part) for 48 and 24 beams. The coefficients are calculated from beamspace tissue data. The point target ROIs consist of a point target and some speckle, while the speckle ROIs only consist of speckle. The two figures have different axes to bring out the details of the progress of the correlation coefficient.

the profile with the minimum width, and the lower part displays the profile with the maximum width. The profile with minimum width represents the smallest size of the point target while the profile with maximum width represents the largest size of the point target.

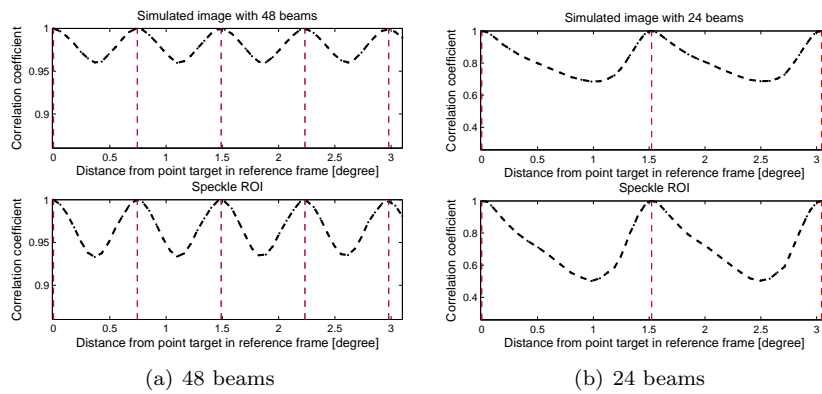


Figure 7.8: Correlation coefficient for the simulated images calculated by point target ROI (upper part) and speckle ROI (lower part) for 48 and 24 beams. Further explanation of the behavior of the figure is as in Figure 7.7.

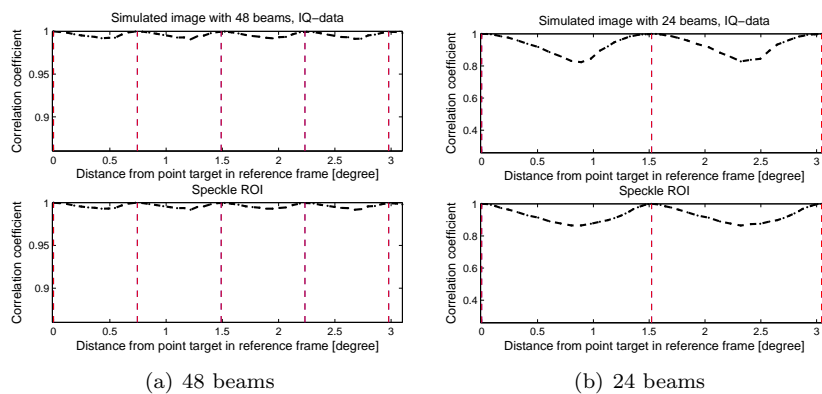


Figure 7.9: Correlation coefficient for the simulated images calculated by point target ROI (upper part) and speckle ROI (lower part) for 48 and 24 beams. Further explanation of the behavior of the figure is as in Figure 7.7.

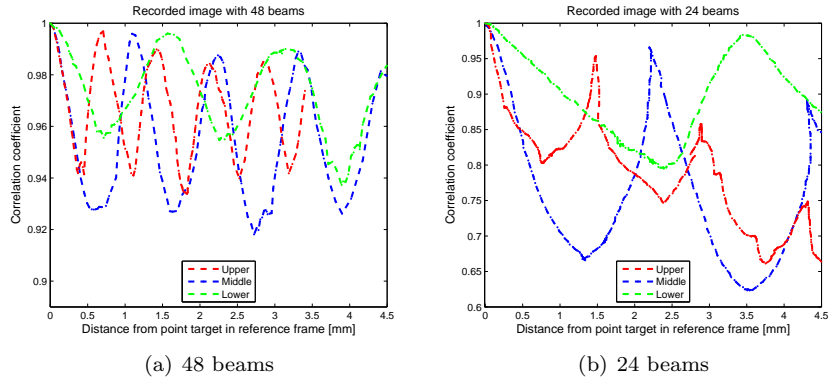


Figure 7.10: Correlation coefficient for three different point targets in the recorded images with 48 and 24 beams. The red graph shows the coefficient for the upper point target, the blue shows the middle point target and the green shows the lower point target. The two figures have different axes to bring out the details of the progress of the correlation coefficient.

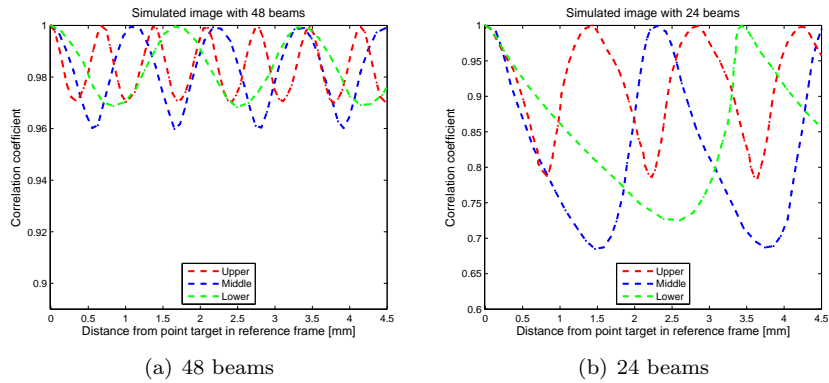


Figure 7.11: Correlation coefficient for three different point targets in the simulated images with 48 and 24 beams. Further explanation of the behavior of the figure is as in Figure 7.10.

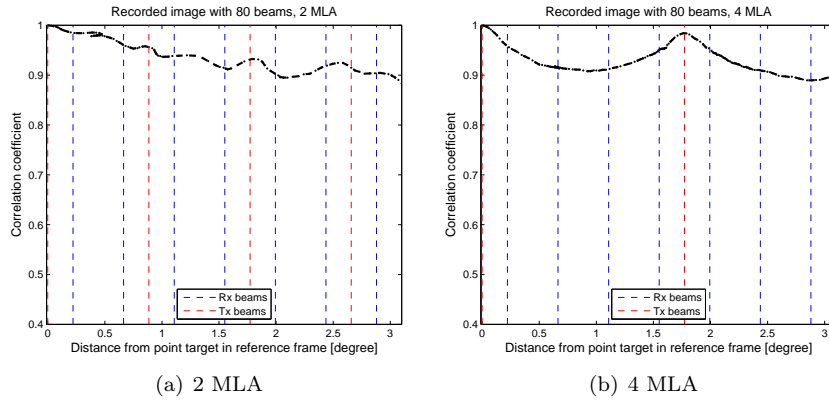


Figure 7.12: Correlation coefficient for the scanned images with 2 and 4 MLA and with 80 receive beams. The correlation coefficient is determined by comparing a ROI, containing a point target, from a reference frame with the corresponding ROIs from the other frames. Tx and Rx beams stands for transmit and receive beams and illustrates where the beams are located related to the distance from the point target in the reference frame.

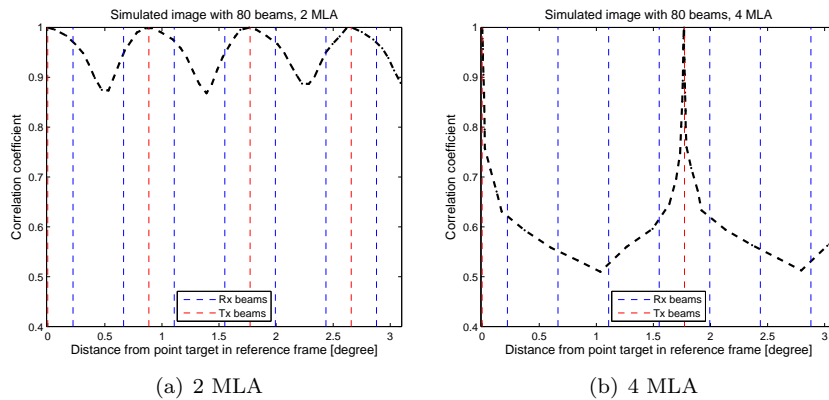


Figure 7.13: Correlation coefficient for the simulated images with 2 and 4 MLA and with 80 receive beams. Further explanation of the behavior of the figure is as in Figure 7.12.

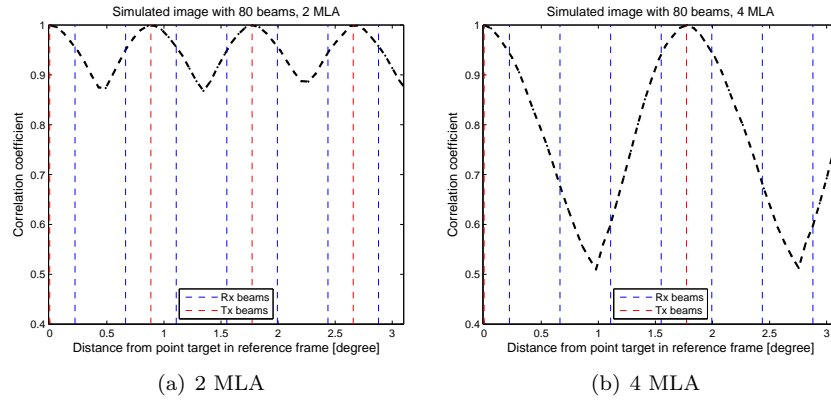


Figure 7.14: Correlation coefficient for the simulated images with 2 and 4 MLA and with receive 80 beams. The distance is measured by applying that the point target moves an equal distance for each frame. Further explanation of the behavior of the figure is as in Figure 7.12.

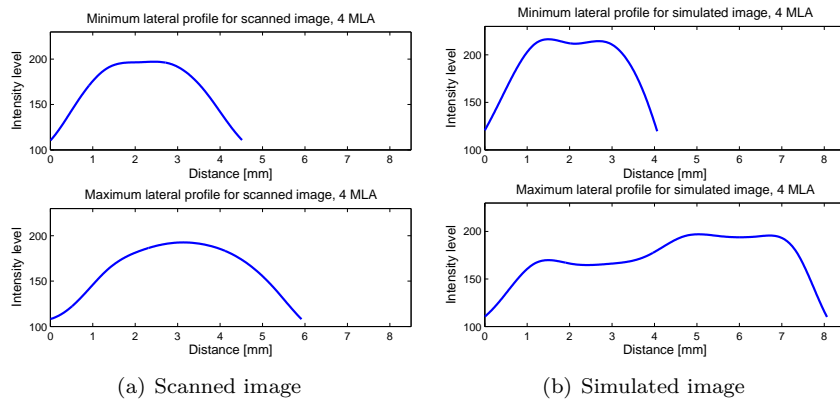


Figure 7.15: Lateral minimum and maximum profiles for the scanned and simulated image with 4 MLA. The upper part of each figure displays the profiles with the minimum width, and the lower part displays the profiles with the maximum width.

7.2 ProbeContact

Figure 7.16 shows the lateral power spectrum for the four cases that was presented in Section 6.2.1. The spectra are all calculated from the same image and the same frame.

Figure 7.17 also displays the lateral power spectrum for the four cases, but now the normalized Fourier transform has been used in the calculations. The calculation of the spectrum in case 1, using the Welch method, has not been changed.

Figure 7.18 shows the 2D Fourier transform of the region close to focus together with lateral and radial power spectrum marked with mean frequency and bandwidth. The lateral and radial spectrum are derived by averaging over the 2D power spectrum.

The output from the ProbeContact algorithm gives a "Probe contact map". This is a histogram visualization of the lateral power spectrum. It also displays the effective aperture parameter given in percent. The Probe contact maps for the different cases are shown in Figure 7.19.

Table 7.2 summarizes the mean frequency and bandwidth for the different cases where the two parameters are derived from the same frame as the power spectra in Figure 7.16 - 7.19 are calculated from. The calculated mean frequency and bandwidth use Eq. 6.4 and 6.5, respectively. Both parameters are expressed in meters since spatial frequencies are evaluated. Figure 7.20 shows mean frequency and bandwidth with increasing frame number for the four cases.

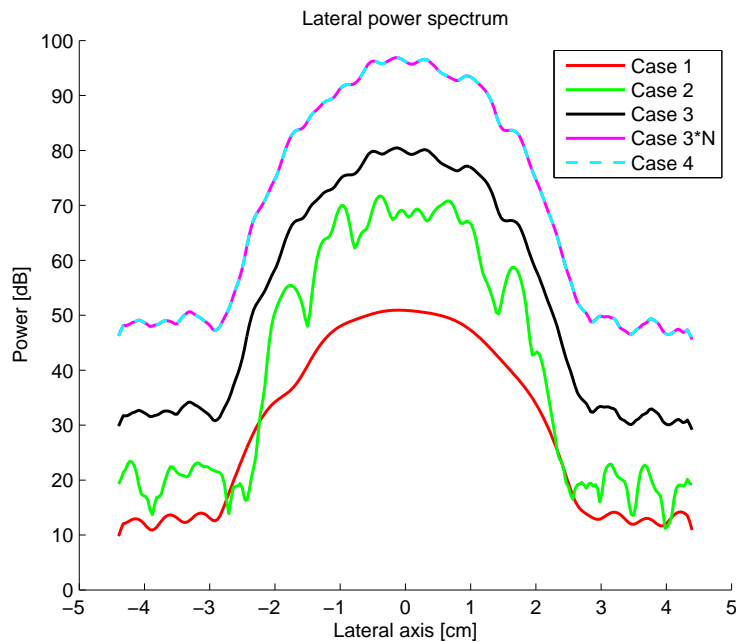


Figure 7.16: Lateral power spectrum for the four cases and in addition a spectrum of N times case 3.

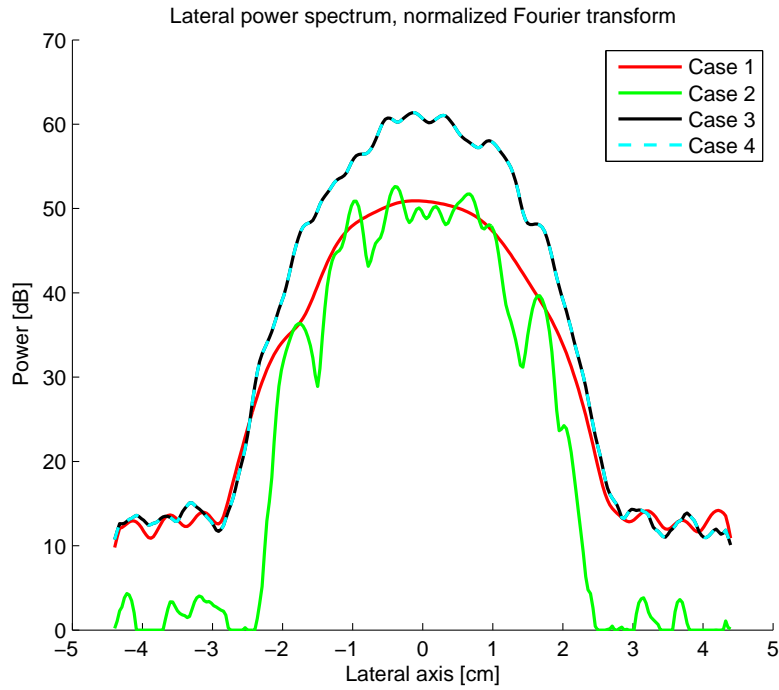


Figure 7.17: Lateral power spectrum for the four cases when normalized Fourier transform has been used in the calculations. The calculation of the spectrum in case 1, using the Welch method, has not been changed.

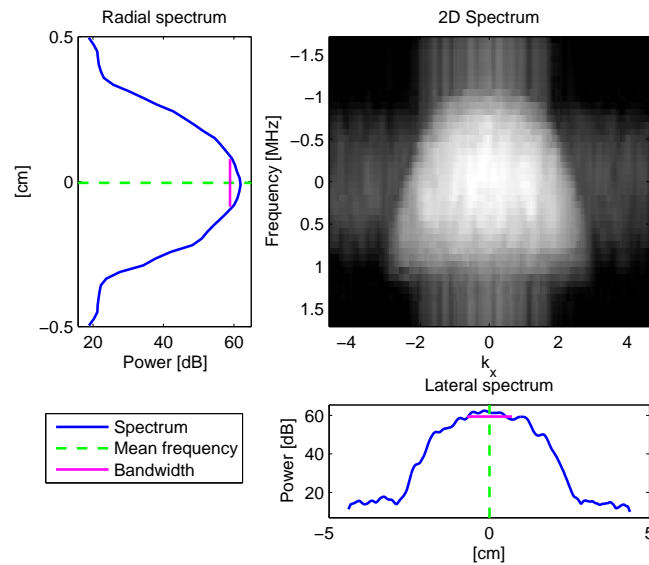


Figure 7.18: The 2D Fourier transform of the region close to focus together with lateral and radial power spectrum marked with mean frequency and bandwidth. The lateral and radial spectrum are derived by averaging over the 2D power spectrum.

Table 7.2: Calculated mean frequency and bandwidth for the four cases and for a specific frame.

Case	Mean frequency [mm]	Bandwidth [cm]
1	-0.1942	1.4350
2	-0.2228	1.3532
3	0.2589	1.3359
4	0.2589	1.3359

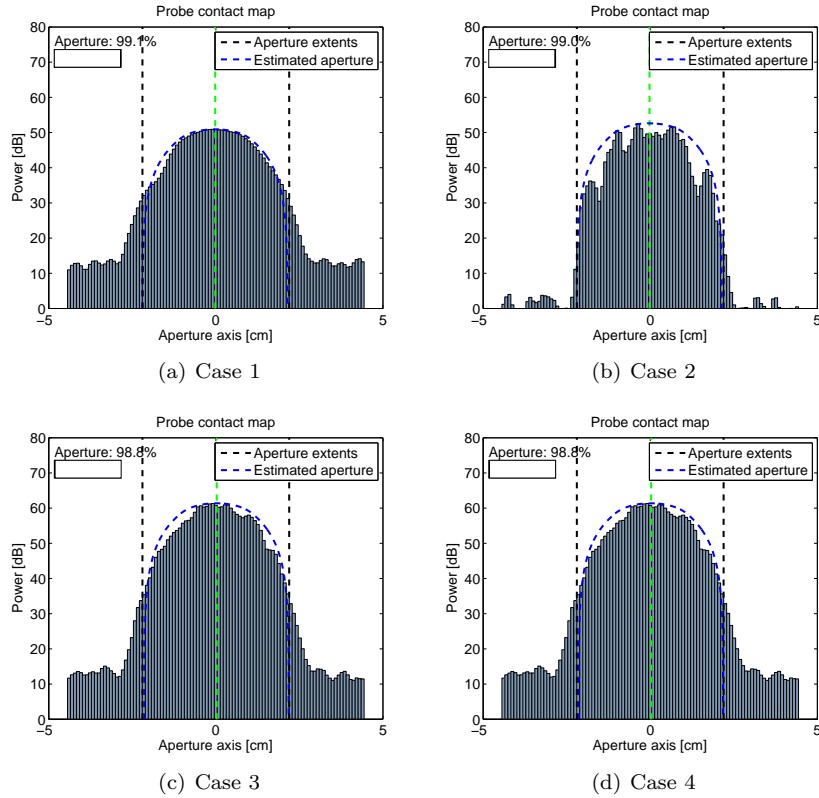
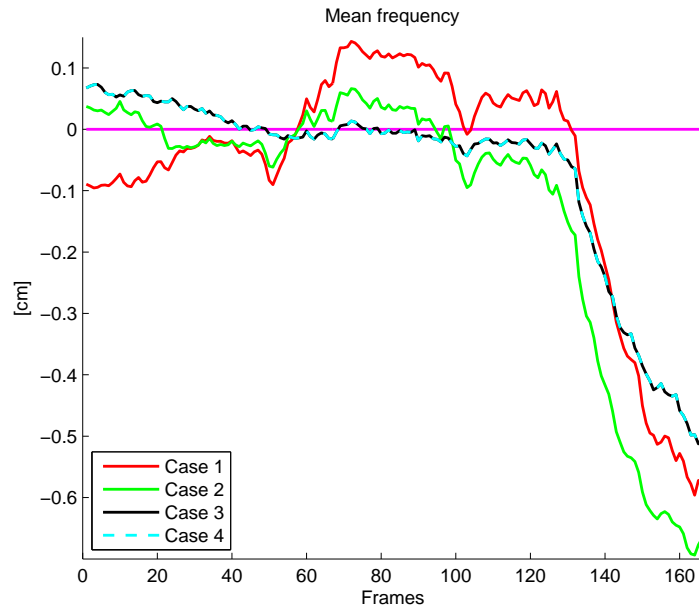
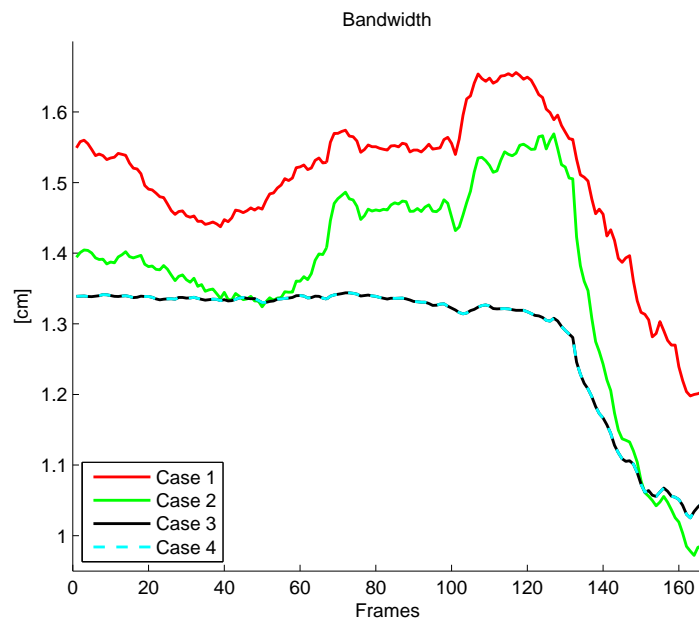


Figure 7.19: Power spectrum map for the four cases. The map is a histogram visualization of the lateral power spectrum. It also displays the effective aperture parameter given in percent. The dotted green line indicates the mean frequency.



(a) Mean frequency



(b) Bandwidth

Figure 7.20: Mean frequency and bandwidth with increasing frame number for the four cases.

Chapter 8

Discussion

8.1 Spatial Variance

One of the purposes of this study was to objectively evaluate the spatial variance in the image. To be able to give a good evaluation of the spatial variance, it has been tested for a variety of scenarios.

8.1.1 Different beam densities

Figure 7.1(a) shows the correlation coefficient for a recorded image with 81 beams. It displays a constantly falling curve. The decrease in correlation coefficient is probably arisen from the fact that the recording is done manually and consequently, it has not been accomplished to retain in the exact same 2D plane for the entire recording. Figure 7.1(b) displays a graph shaped like a wave with tops located at every beam. These tops correspond well with the position of the point target when it is placed precisely in a beam, and it is expected that the correlation coefficient will be high at these points. When a point target is between two beams, it will laterally smear out, and as seen in the figures, the correlation coefficient will decrease.

The results from the simulated images with the same beam densities, shown in Figure 7.2, correspond well with the results from the scanned images in Figure 7.1. When the correlation coefficient is 1, we have spatial invariance. This holds only when the point target is placed in a beam. When the correlation coefficient decreases between the beams, the spatial variance increases. The image gets more and more spatially variant as the beam density decreases.

Figure 7.1(c) and 7.1(d), and Figure 7.2(c) and 7.2(d) for the simulated case, show the correlation coefficient when the beam density is relatively low. In Figure 7.1(d), it is also shown that the shape of the graph is dramatically changed, and the correlation coefficient decreases without particularly moving further away from the reference frame when the point target is close to a beam. This is also the case for Figure 7.2(d). It seems like the point target moves more slowly when passing a beam. This concurs with the profile plot for 19 beams in Figure 7.4(b). By comparison of this profile plot with the corresponding plot for 81 beams, Figure 7.4(a), it can be seen that the pattern of the succeeding profiles for 19 beams will change, and the point target in the image will not move with equal distance even though each frame is tilted with the same degree for every frame. A movie of the discussed point target has been added to the

zip file attached in the electronic version of the thesis. More details can be found in Appendix C.

As can be seen in Table 7.1, Figure 7.1(d) is also the only one of the four plots in Figure 7.1 that represents an image that do not fulfill the Nyquist sampling theorem. The same holds for Figure 7.2(d) for the simulated images. Sampling below the Nyquist limit will result in aliasing, and the signal will not be reconstructed properly. This will influence the regions between the beams in the image, and these areas will be constructed by interpolation of the nearby beam fields. The movement of the point target will be exactly intercepted when the point target is close to a beam. But between the beams, detailed movements will not be registered, and the point target will only be imaged with exact details when it is getting closer to a new beam again. This concurs with the movie and the calculated correlation coefficients.

Figure 7.2(c) shows that the shape of the correlation coefficient is also slightly altered with pointed tops at the location of the beams even though the beam density is not below the Nyquist sampling limit. This figure represents an image with a beam density just above the limit, and the point target is influenced by the low beam density, but only to a minor degree.

As for Figure 7.2, Figure 7.3 shows the correlation coefficient for the simulated images. Instead of measuring the distance as explained in Section 5.2, the distance is calculated by applying that the point target moves an equal distance for each frame since, for the simulated case, each frame is tilted exactly the same amount of degrees. This figure shows that all plots are shaped like smooth waves, even the plots with low beam densities. If it had not been for the discovery of the irregular movements of the point target for low beam densities, it would have been easy to presume that the results in Figure 7.3 are more accurate than the ones in Figure 7.2 based on that the image is tilted with the same distance for every frame. Figure 7.3 gives an accurate indication of the changing correlation coefficient for high beam densities, but it does not show the changes in the movement of the point target for low beam density. However, the spatial variance is equally high for Figure 7.3.

8.1.2 IQ-data

By comparing Figure 7.5(a) and 7.5(b), and Figure 7.6(a) and 7.6(b), it is observed that the correlation coefficients are higher for Figure 7.5(b) and 7.6(b). In addition, the shape of the correlation coefficient calculated from IQ-data is different from the coefficient calculated from beamspace tissue data. If IQ-data is denoted as $s_{IQ}(x, z)$, the beamspace tissue data will be $20 \log_{10}(|s_{IQ}(x, z)|)$, and it is natural that the correlation coefficient calculations will be influenced by this difference. The figures show that IQ-data calculations give lower spatial variance than beamspace tissue data. Further evaluation of the differences between IQ-data and beamspace tissue data has not been emphasized.

8.1.3 Speckle pattern

By comparison of the correlation coefficient calculated from a ROI which includes the point target and a ROI which only consists of speckle, it can be seen from Figure 7.7 and 7.8 that the results are fairly similar. The main difference, for both the scanned and the simulated images, is that the correlation

coefficient for the speckle ROI decreases more than for the point target ROI. In Figure 7.9, where IQ-data has been used to calculate the correlation coefficient, this difference is close to being gone. This can be explained by looking at the correlation coefficient calculations from IQ-data. Appendix D shows that the normalized correlation coefficient for one single point target is the same as the normalized correlation coefficient for a sum of uncorrelated point targets. Our speckle ROI is the sum of uncorrelated point targets, and the single point target can be approximated to be our point target ROI which consists of a strong point target with surrounding speckle. Figure 7.9 should accordingly give similar results for the point target ROI and speckle ROI.

But for Figure 7.7 and 7.8, the correlation coefficient is calculated from beamspace tissue data and this will influence the calculations. In Appendix D, it was shown that

$$\langle \sum_{n_1} s_{n_1}(x, z) \sum_{n_2} s_{n_2}(x + \Delta x, z + \Delta z) \rangle \quad (\text{Eq. D.8})$$

could be expressed as

$$\langle \sum_n s_n(x, z) s_n^*(x + \Delta x, z + \Delta z) \rangle \quad (\text{Eq. D.16})$$

and this corresponded to that the correlation coefficient was the same for a single point target and for a sum of uncorrelated point targets. This is no longer the case since our signal will be $20 \log_{10}(|s(x, z)|)$, and the normalized correlation coefficient should not be the same for a point target ROI and a speckle ROI when using beamspace tissue data.

If the spatial variance is compared, it must be assured that only speckle ROIs or point target ROIs are used for all frames. This is when the spatial variance is calculated from beamspace tissue data. This assumption is no longer necessary if the spatial variance is calculated from IQ-data.

8.1.4 Various point targets

Three different point targets in the same image have been evaluated related to the correlation coefficient, and Figure 7.10 and 7.11 show that the three point targets all have the same shape but they vary in frequency. This is expected. Since our images are generated by sector scans, the beams are very close together in the upper part of the image and more spread out in the lower part of the image. The point target in the upper part of the image will then be located in a beam more frequently than the other point targets if the distances are compared in meters. Point targets in the lower part of the image will then be more influenced by low beam densities compared to point targets in the upper part of the image.

From Figure 7.11 it can be seen that the minimum correlation coefficient value varies for the different point targets. The upper point target has the lowest decrease in correlation coefficient. This is understandable since the upper part of the image is where there is least distance between the beams. It is then expected that the lowest point target should have the lowest correlation coefficient value, but as can be seen from the figure, this is not the case. The reason for this is that the correlation calculations compare two ROIs consisting of a point target, but also consisting of some speckle. The intensity level of the image will decrease with increasing depth due to attenuation, and the lower part of the image will have a lower intensity level, including the speckle. The point target will still change, but the visibility of the fluctuation of the speckle will be reduced and this will result in less decrease in the correlation value.

8.1.5 MLA

When MLA is used, it is received more beams than it is transmitted. Figure 7.12 and 7.13 show that tops only appear in the correlation coefficient plots when the point target is located near a transmit beam and not when it is near a receive beam. MLA utilizes that an image can be created by shooting few transmit beams, but as seen from the figures, it greatly increases the spatial variance. This was expected. As mentioned in Section 5.1, an imaging system needs to consist of beams that are equal in shape and which are equally spaced to be spatially invariant. The Nyquist sampling theorem must also be satisfied. When MLA is used, the shape and the spacing of the beams will vary. In addition, it can be seen from Table 7.1 that the Nyquist sampling theorem is not satisfied for 4 MLA. The correlation coefficient is then especially low for 4 MLA which corresponds to a high spatial variance. Figure 7.13(b) has a beam density of 80 beams, but since 4 MLA has been used, the correlation coefficient is as low as for Figure 7.2(d), which has a beam density of 19 beams.

There is an alternative method for use of parallel beamforming, but without the large spatial variance. The Synthetic Transmit Beams (STB) method suggests to create synthetic transmit beams in the direction of each receive beam, and this leads to images with less spatial variance compared to MLA images [3].

Figure 7.14 shows the correlation coefficient for the same properties as for Figure 7.13, but the distance is calculated by applying that the point target moves an equal distance for each frame. It can be seen that Figure 7.14(a) is similar to Figure 7.13(a). This is not the case for Figure 7.14(b) and 7.13(b). As for the scenario with single line acquisition and 19 beams, the coefficient in Figure 7.14(b) indicates that the point target moves more slowly when passing a beam. They also resembles by not fulfilling the Nyquist sampling theorem. Figure 7.2(d) with 19 beams and Figure 7.14(a) with 4 MLA show that the shape of the correlation coefficient greatly changes when the Nyquist sampling theorem is not satisfied, and the spatial variance becomes very high.

By comparing Figure 7.12(a) and 7.13(a), it can be seen that the correlation coefficient between two transmit beams is much lower for Figure 7.13(a). This is even more evident for Figure 7.12(b) and 7.13(b). The difference may come from the fact that the scanned images are recorded manually which causes irregularities. It can also be explained by studying the profile with minimum width and the profile with maximum width for the scanned and the simulated image. This is shown in Figure 7.15 where 4 MLA has been used. The profile with minimum width represents the smallest size of the point target while the profile with maximum width represents the largest size of the point target. Since the difference between the minimum width profile and the maximum width profile for the scanned image is quite small, there is only a small difference between the two profiles, and with that only a small difference between the smallest and largest point target, and the correlation coefficient will not decrease very much between two adjacent beams. But for the simulated case, the minimum width profile is much smaller than the maximum width profile which results in a greater size difference between the smallest and the largest point target, and the correlation will decrease more for the simulated image than for the scanned. The width of the maximum profile for the simulated image is surprisingly large.

8.2 ProbeContact

The other main purpose of this study was to evaluate different power spectra related to the ProbeContact algorithm. It can be seen from Figure 7.16 that the lateral power spectrum for case 1 has reduced noise compared to case 2. But at the same time this spectrum has few details of the local features. This was expected due to the properties of the Welch method.

When averaging a function followed by the Fourier transform, the spectrum will have a high variance but reduced noise, while performing Fourier transform followed by averaging will give a smooth spectrum but the signal to noise ratio (SNR) will be reduced [7]. It is then expected that the spectra from case 1 and 2 have higher variance than the spectra from case 3 and 4. But the spectrum from case 1 is also smoothed by the Welch method, and as can be seen in the figure, the spectrum from case 2 has the highest variance compared to all the other cases. But at the same time, the spectrum from case 2 has also very low sidelobe levels. This is seen in Figure 7.17.

In Figure 7.16, the power spectrum from case 2 does not match the power spectrum from case 3. This was expected based on Eq. 6.1. It was also suggested that the power spectrum for case 3 would overall have higher power level than for case 2. This is in accordance with the figure.

From Eq. 6.2, it was determined that the lateral power spectrum for case 4 should be equal to N times case 3, $NG_3(k_x)$. This corresponds well with the figure where the lateral spectrum from case 4 matches exactly with N times the lateral spectrum from case 3.

Figure 7.17 shows the lateral power spectra for the four cases when normalized Fourier transform has been used in the calculations. The figure shows that the lateral power spectrum, calculated with normalized Fourier transform, for case 3 is equal to the corresponding power spectrum for case 4, just as given in Eq. 6.3. The average power level is different for case 1 and 2 compared to 3 and 4. This is not unexpected since averaging in space can be viewed as a lowpass filter while averaging in frequency domain can be viewed as a bandpass filter. This will naturally introduce some differences.

By looking at the 2D power spectrum in Figure 7.18, it can be seen that the spectrum is concentrated in the middle of the image and bounded in both directions. This corresponds well with the k -space theory discussed in Section 2.3 and with Figure 2.7, where the PSF in k -space is limited in both directions. The 2D spectrum in Figure 7.18 contains some noise on the sides as well.

Figure 7.19 shows the probe contact maps for the four cases when normalized DFT has been used in the calculations. Figure 7.19(c) and 7.19(d) are exactly the same. This is expected when Figure 7.17 showed that the lateral power spectra for case 3 and 4 are equal when normalized Fourier transform is used. In addition, the mean frequency and bandwidth are the same. It has then no influence on the output of the algorithm whether case 3 or case 4 are used. This requires calculations with normalized Fourier transform. When case 3 and 4 are evaluated further in the discussion, only case 4 will be mentioned, though it applies for both case 3 and 4.

The effective aperture parameter, displayed in percent, is shown in the upper left corner of each probe contact map. This parameter is calculated by use of the mean frequency, and it is reasonable that Figure 7.19(a) has the highest percent, 99.1%, since Table 7.2 shows that case 1 has the lowest mean

frequency. Case 4 has the highest mean frequency, and correspondingly has the lowest effective aperture percent shown in 7.19(d), that is 98.8%. Even so, the percent parameter is almost the same for all cases.

The probe contact maps in Figure 7.19 is rendered for a specific frame. Figure 7.20 shows the calculated mean frequency and bandwidth for all frames. Case 3 and 4 will also here give equal results. By looking at Figure 7.20(a), it can be seen that most parts of the mean frequency plot for case 1 and case 2 are quite similar in their shape, but with different levels. This is also the case for the bandwidth in Figure 7.20(b). A high effective aperture percent is achieved by having a mean frequency as close as possible to zero. So, even though the shape of the mean frequency is the same, the distance from zero is different for the two cases and will result in different effective apertures.

By first calculating the power spectrum by Fourier transformation and next averaging the power spectrum, the variance in the spectrum is reduced. This gives a good estimate of the spectrum and the mean frequency is more stable. This concurs with the mean frequency for case 4.

Figure 7.20(b) shows the bandwidth with increasing frame number for all cases. It is seen from the figure that the bandwidth for case 4 is smoother than for case 1 and 2. The calculated bandwidth is dependent of the mean frequency, cf. Eq. 6.5, and it is likely that the smooth bandwidth for case 4 when the contact is good arises since the mean frequency for case 4 is also relatively smooth. In addition, the bandwidth is more closely connected to the variance in the power spectrum than the mean frequency.

The ProbeContact algorithm to date does not use the bandwidth in its calculations, so the advantage of a smooth bandwidth does not influence the output of the present algorithm. Rearranging the order of averaging and Fourier transformation will have an impact on the calculated probe contact since the mean frequency varies for the four cases, but the differences are not huge. The biggest difference in Figure 7.20(a) is at beam number 79 where the effective aperture parameter will display 94.2% for case 1 and 99.9% for case 4. If the bandwidth is incorporated in the ProbeContact algorithm, it will influence the calculated probe contact. Case 3 and 4 may be preferable compared to the other cases because of the reduced variance which gives a smooth mean frequency and bandwidth for various frames.

Part IV

Conclusion

Chapter 9

Conclusion

As the evolution of technology moves forward, the ultrasound scanners are getting smaller and more complex. It is then increasingly important to have a system that can give the user feedback on the quality of the current image.

The purpose of the present study was to objectively evaluate the image quality of phantom images. The study included only phantom images and not clinical images. This was done to limit the scope of the thesis. A great amount of the study was based on the existing image analysis system which evaluates various image quality parameters.

A new parameter related to the image quality system was evaluated in this thesis; spatial variance. An algorithm was made to objectively evaluate the spatial variance for different beam densities, IQ-data, speckle pattern, various point targets and for MLA. Correlation coefficient was used as a measure of spatial variance. From the results, it can be concluded that an image gets more and more spatially variant as the beam density decreases. It has also been shown that the correlation coefficient is generally higher, that is the spatial variance is lower, when the correlation coefficient is calculated from IQ-data compared to calculations from beamspace tissue data. If spatial variance should be compared, it is important with consistency and that every calculation for the different cases is either from IQ-data or from beamspace tissue data. The calculation of spatial variance for a region mainly consisting of a point target and for a region only consisting of speckle, gives fairly similar results but with a small difference in the measured correlation coefficient. The results also show that the various point targets will give the same pattern for changes in spatial variance, and MLA will greatly reduce the spatial variance. Based on figures and evaluating a movie of the point target, it can be concluded that the movement of a point target changes when the beam density goes below the Nyquist sampling limit. The point target will appear to move more slowly when passing a beam since the region between two beams is undersampled. This effect will be expressed in the correlation coefficient plots by changes in the shape of the coefficient.

Altogether, it can be concluded that the algorithm gives a good evaluation of the spatial variance of a phantom image. It does require the image to be recorded in a specific way, but it gives valuable information of the spatial variance for a variety of settings. It seems acceptable to use the correlation coefficient as a measure of spatial variance.

The other main purpose of this study was to incorporate the ProbeContact algorithm in the system and to evaluate different power spectrum calculations. Four different ways of calculating the lateral power spectrum were evaluated in this thesis. It can be seen from the results that the different calculations give mostly different power spectra. An exception from this are case 3 and 4 which will be equal as long as normalized Fourier transform is used in the calculations. Case 3 performs 1 dimensional Fourier transform, takes absolute value and square of the variables, followed by averaging while case 4 performs the same calculations, but where 2 dimensional Fourier transform is used instead. The different power spectrum calculations will give different output from the ProbeContact algorithm, but the differences are small and all methods give tolerable results. The differences that do exist can be seen in the calculations of the mean frequency and bandwidth for all frames. The mean frequency and bandwidth is smoother for case 3 and 4 (Fourier transform before averaging), than for case 1 and 2 (averaging before Fourier transform). This is because case 3 and 4 have a low variance in the power spectrum estimate. It may be inferred that case 3 and 4 should be used in the algorithm rather than case 1 and 2 based on the low variance of the power spectrum and the smooth mean frequency. The ProbeContact algorithm to date does not use bandwidth in its calculations, but if it is incorporated in the algorithm, case 3 and 4 have also the advantage of a smooth bandwidth. This is suggested with the reservations of basic settings, for instance that rectangular aperture is used.

In conclusion, it can be said that the image analysis system is now stronger with the spatial variance parameter, but it requires a specific way of recording the image. The system is a good tool for evaluation of various parameters related to image quality and can also be used for performance testing of the scanner. The system is improved by use of the ProbeContact algorithm which gives a good indication of the image quality based on the acoustic contact of the probe. Rearranging the order of averaging and Fourier transformation will have an impact on the calculated probe contact, but the differences are not huge. Using 1D (in the lateral direction) or 2D Fourier transform before averaging will not have any impact of the resulting power spectrum as long as normalized DFT is used.

The final goal in the future is to objectively evaluate the image quality in clinical images. Even though the image analysis system is limited to phantom images, the thesis is a step in the right direction in the process of achieving that goal. The image analysis system can be a good basis for others to work further on.

9.1 Future Work

The following are proposals for further work on a system that objectively evaluates the image quality in ultrasound images:

- **More parameters evaluated by the system.** Increasing the number of parameters will give a more reliable measurement of the image quality. Relevant parameters can be edge sharpness, different noise parameters and speckle characteristics.

- **Give a score of the image quality in an image.** After the evaluation of the parameters is completed, they should be ranked and given a score where important quality parameters are more weighted than others. The system gives a total score of the quality of the image.
- **Transmit to clinical images.** The system should be adapted to clinical images. This is a comprehensive task since most methods used in the image analysis system are not easily transferable to clinical images due to that they are dependent of point targets. Spatial variance could perhaps be measured by comparing how similar radial edges change in different places in the image. A disadvantage of this is that radial edges are not easily measured accurately.

References

- [1] Martin E. Anderson and Gregg E. Trahey. A seminar on k-space applied to medical ultrasound. Department of Biomedical Engineering, Duke University, April 2000.
- [2] Jacob Beutel, Steven C. Horii, and Yongmin Kim. *Handbook of Medical Imaging: Display and Pacs*. SPIE Press, 2000.
- [3] Tore Grüner Bjåstad. *High frame rate ultrasound imaging using parallel beamforming*. PhD thesis, NTNU, 2009.
- [4] Patrizio Campisi and Karen Egiazarian. *Blind Image Deconvolution: Theory and Applications*. CRC Press, 2007.
- [5] CIRS, Tissue Simulations & Phantom Technology. *CIRS Model 40 data sheet, General Purpose Multi-Tissue Ultrasound Phantom*.
- [6] V. Devanathan. *Angular Momentum Techniques in Quantum Mechanics*. Kluwer Academic Publishers, 1999.
- [7] Azima DLI. Introduction To Machine Vibration Online Text Book. www.dliengineering.com/vibman/default.htm. [Online; visited 2nd May 2009].
- [8] Nicholas M. Gibson, Nicholas J. Dudley, and Kate Griffith. A computerised quality control testing system for B-mode ultrasound. *Ultrasound in Med. & Biol.*, 27, No.12:1697–1711, 2001.
- [9] Wayne R. Hedrick, David L. Hykes, and Dale E. Starchman. *Ultrasound Physics and Instrumentation*. Andrew Allen, 2005.
- [10] Technical University of Denmark . Jørgen Arendt Jensen. Field II Simulation Program. <http://server.oersted.dtu.dk/personal/jaj/field/>. [Online; visited 12th March 2009].
- [11] Johan Kirkhorn. Introduction to IQ-demodulation of RF-data. IFBT, NTNU, September 15 1999.
- [12] Lasse Løvstakken, Fredrik Orderud, and Hans Torp. Real-time Indication of Acoustic Window for Phased-Array Transducers in Ultrasound Imaging. *2007 IEEE Ultrasonics Symposium*, pages 1549–1552, 2007.
- [13] David S. Moore. *The basic practice of statistics*. W. H. Freeman and Company, 1995.

- [14] John G. Proakis and Dimitris G. Manolakis. *Digital Signal Processing*. Pearson Prentice Hall, 2007.
- [15] BORES Signal Processing. Advanced DSP - FFT windows: coherent power gain.
http://www.bores.com/courses/advanced/windows/10_cpg.htm. [Online; visited 12th May 2009].
- [16] Bjørn Angelsen and Hans Torp. *Ultrasound Imaging - Waves, Signals and Signal Processing in Medical Ultrasonics, Vol I & Vol II*. Emantec AS, 2000.
- [17] John L. Semmlow. *Biosignal and biomedical image processing : MATLAB-based applications*. Marcel Dekker, Inc., 2004.
- [18] David P. Shattuck, Marc D. Weinshenker, Stephen W. Smith, and Olaf T. von Ramm. Explososcan: A parallel processing technique for high speed ultrasound imaging with linear phased arrays. *Journal of the Acoustical Society of America*, 75, 4:1273–1282, 1984.
- [19] K. Kirk Shung. *Diagnostic Ultrasound: Imaging and Blood Flow Measurements*. CRC, 2005.
- [20] Cecilie Øinæs Simpson. Objective Image Quality Metrics for Ultrasound Imaging. Project assignment, NTNU, Autumn 2008.
- [21] J.M. Thijssen, M.C. van Wijk, and M.H.M. Cuyppers. Performance testing of medical echo/Doppler equipment. *European Journal of Ultrasound*, 15:151–164, 2002.
- [22] Johan M. Thijssen, Gert Weijers, and Chris L. De Korte. Objective performance testing and quality assurance of medical ultrasound equipment. *Ultrasound in Med. & Biol.*, 33, No. 3:460–471, 2007.
- [23] Hans Torp and Jonas Crosby. RF-data akkvisisjon og prosessering, Øving 7, TTK4165 Signalbehandlingsmetoder i medisinsk billedannelse, 2008.
- [24] Kutay F. Üstuner and Gregory L. Holley. Ultrasound Imaging System Performance Assessment. AAPM 45th Annual Meeting, Aug.10-14 2003.
- [25] Vingmed. *System 5 Service Manual*, rev. c edition.
- [26] William F. Walker and Gregg E. Trahey. *1995 IEEE Ultrasonics Symposium: proceedings, Paper: The application of k-space in medical ultrasound*, volume 2. 1995.
- [27] Wikipedia. Image: Convolution Illustrated.
http://en.wikipedia.org/wiki/Image:Convolution_Illustrated_eng.png. [Online; visited 7th April 2009].
- [28] J.N. Wright. Image formation in diagnostic ultrasound. In *Short Course, IEEE International Ultrasonics Symposium*, 1997.

Part V
Appendices

Appendix A

Mathematical Relations in ProbeContact

A.1 Mathematical Equations Used in the Four Cases

Table A.1 summarizes the mathematical equations used in the four cases when evaluating the power spectrum in ProbeContact, that is 1D, normalized 1D and 2D DFT definitions together with the 1D averaging equation for discrete signals.

Table A.1: DFT and average definition(s). For DFT we have that $k_x = 0, 1, 2, \dots, M-1$ and $k_z = 0, 1, 2, \dots, N-1$.

<i>Name</i>	<i>Expression</i>	<i>Eq. no.</i>
1D DFT	$F(k_x) = \sum_{x=0}^{M-1} f(x) e^{-j2\pi \frac{k_x x}{M}}$	(A.1)
	$f(x) = \frac{1}{M} \sum_{k_x=0}^{M-1} F(k_x) e^{j2\pi \frac{k_x x}{M}}$	(A.2)
2D DFT	$F(k_x, k_z) = \sum_{x=0}^{M-1} \sum_{z=0}^{N-1} f(x, z) e^{-j2\pi (\frac{k_x x}{M} + \frac{k_z z}{N})}$	(A.3)
	$f(x, z) = \frac{1}{NM} \sum_{k_x=0}^{M-1} \sum_{k_z=0}^{N-1} F(k_x, k_z) e^{j2\pi (\frac{k_x x}{M} + \frac{k_z z}{N})}$	(A.4)
Normalized 1D DFT	$F(k_x) = \frac{1}{\sqrt{M}} \sum_{x=0}^{M-1} f(x) e^{-j2\pi \frac{k_x x}{M}}$	(A.5)
	$f(x) = \frac{1}{\sqrt{M}} \sum_{k_x=0}^{M-1} F(k_x) e^{j2\pi \frac{k_x x}{M}}$	(A.6)
Averaging	$\bar{f} = \frac{1}{N'} \sum_{i=1}^{N'} f(x_i)$	(A.7)

A.2 Relation Between Averaging and 1D FT

By neglecting the absolute value and taking square of the variables when calculating the spectra, the calculations are simplified. Case 2 is then defined as averaging a function followed by 1D Fourier transform, while case 3 is defined as performing 1D Fourier transform followed by averaging. Since no absolute value or taking square of the variables are done, the spectra are denoted $S(k_x)$ and not $G(k_x)$ which is the denotation for power spectrum.

A region in the image close to the focus is defined as $s(x, z)$. This region is the same for all the cases. M is the size of the region in the radial direction, while N , though not used in this section, is the size of the region in the lateral direction. N' is the number of elements when calculating the average. The region is Fourier transformed in the lateral direction.

By using the equations in Table A.1, case 3 can be expressed as

$$S_3(k_x) = \frac{1}{N'} \sum_{i=1}^{N'} \left[\sum_{x=0}^{M-1} s(x, z_i) e^{-j2\pi \frac{k_x x}{M}} \right] \quad (\text{A.8})$$

In the same manner, case 2 can be expressed as

$$S_2(k_x) = \sum_{x=0}^{M-1} \left[\frac{1}{N'} \sum_{i=1}^{N'} s(x, z_i) \right] e^{-j2\pi \frac{k_x x}{M}} \quad (\text{A.9})$$

By rearranging the elements in $S_2(k_x)$, we get

$$S_2(k_x) = \frac{1}{N'} \sum_{x=0}^{M-1} \sum_{i=1}^{N'} s(x, z_i) e^{-j2\pi \frac{k_x x}{M}} \quad (\text{A.10})$$

$$= \frac{1}{N'} \sum_{i=1}^{N'} \left[\sum_{x=0}^{M-1} s(x, z_i) e^{-j2\pi \frac{k_x x}{M}} \right] \quad (\text{A.11})$$

$$= S_3(k_x) \quad (\text{A.12})$$

A.3 Relation Between Averaging and $|1D FT|^2$

Case 2, without any simplifications, is defined as averaging a function followed by 1D Fourier transform and then taking absolute value and square of the variables, while case 3 is defined as performing 1D Fourier transform and then taking absolute value and square of the variables followed by averaging.

Case 3 can be expressed as

$$G_3(k_x) = \frac{1}{N'} \sum_{i=1}^{N'} \left[\left| \sum_{x=0}^{M-1} s(x, z_i) e^{-j2\pi \frac{k_x x}{M}} \right|^2 \right] \quad (\text{A.13})$$

and case 2 can be expressed as

$$G_2(k_x) = \left| \sum_{x=0}^{M-1} \left[\frac{1}{N'} \sum_{i=1}^{N'} s(x, z_i) \right] e^{-j2\pi \frac{k_x x}{M}} \right|^2 \quad (\text{A.14})$$

Section A.3.1 shows that

$$|a + b| \leq |a| + |b| \Rightarrow \left| \sum_{i=1}^I \sum_{j=1}^J a_{ij} \right| \leq \sum_{i=1}^I \left| \sum_{j=1}^J a_{ij} \right|$$

and Section A.3.2 shows that

$$\left(\sum_{i=1}^n a_i \right)^2 = \sum_{i=1}^n a_i^2 + 2 \sum_{i=1}^{n-1} \sum_{j=i+1}^n a_i a_j$$

By changing the order of the elements and by use of these results, we get

$$G_2(k_x) = \left| \frac{1}{N'} \sum_{x=0}^{M-1} \sum_{i=1}^{N'} s(x, z_i) e^{-j2\pi \frac{k_x x}{M}} \right|^2 \quad (\text{A.15})$$

$$= \left| \frac{1}{N'} \sum_{i=1}^{N'} \sum_{x=0}^{M-1} s(x, z_i) e^{-j2\pi \frac{k_x x}{M}} \right|^2 \quad (\text{A.16})$$

$$= \frac{1}{(N')^2} \left| \left(\sum_{i=1}^{N'} \sum_{x=0}^{M-1} s(x, z_i) e^{-j2\pi \frac{k_x x}{M}} \right) \right|^2 \quad (\text{A.17})$$

$$= \frac{1}{(N')^2} \left| \sum_{i=1}^{N'} \left(\sum_{x=0}^{M-1} s(x, z_i) e^{-j2\pi \frac{k_x x}{M}} \right) \right|^2 + 2 \underbrace{\sum_{i=1}^{N'-1} \sum_{l=i+1}^{N'} \left(\sum_{x=0}^{M-1} s(x, z_i) e^{-j2\pi \frac{k_x x}{M}} \right) \left(\sum_{x=0}^{M-1} s(x, z_l) e^{-j2\pi \frac{k_x x}{M}} \right)}_{\alpha} \right| \quad (\text{A.18})$$

$$\leq \frac{1}{(N')^2} \left| \sum_{i=1}^{N'} \left(\sum_{x=0}^{M-1} s(x, z_i) e^{-j2\pi \frac{k_x x}{M}} \right) \right|^2 + \frac{2}{(N')^2} |\alpha| \quad (\text{A.19})$$

$$\leq \frac{1}{(N')^2} \sum_{i=1}^{N'} \left| \sum_{x=0}^{M-1} s(x, z_i) e^{-j2\pi \frac{k_x x}{M}} \right|^2 + \frac{2}{(N')^2} |\alpha| \quad (\text{A.20})$$

$$= \frac{1}{N'} G_3(k_x) + \frac{2}{(N')^2} |\alpha| \quad (\text{A.21})$$

The relation between case 2 and 3 is then

$$G_2(k_x) \leq \frac{1}{N'} G_3(k_x) + \frac{2}{(N')^2} |\alpha| \quad (\text{A.22})$$

where

$$\alpha = \sum_{i=1}^{N'-1} \sum_{l=i+1}^{N'} \left(\sum_{x=0}^{M-1} s(x, z_i) e^{-j2\pi \frac{k_x x}{M}} \right) \left(\sum_{x=0}^{M-1} s(x, z_l) e^{-j2\pi \frac{k_x x}{M}} \right) \quad (\text{A.23})$$

$$= \sum_{i=1}^{N'-1} \sum_{l=i+1}^{N'} S(k_x, z_i) S(k_x, z_l) \quad (\text{A.24})$$

and $S(k_x, z) = \mathcal{F}_x\{s(x, z)\}$. This shows that the two cases are not the same.

A.3.1 Triangular inequality

The triangular inequality can be expressed as

$$|a + b| \leq |a| + |b| \quad (\text{A.25})$$

where a and b can be both real and complex numbers.

The triangular inequality can be applied for summation variables:

$$\left| \sum_{i=1}^I \sum_{j=1}^J a_{ij} \right| = |(a_{11} + a_{12} + \dots + a_{1J}) + (a_{21} + a_{22} + \dots + a_{2J}) + \dots + (a_{I1} + a_{I2} + \dots + a_{IJ})| \quad (\text{A.26})$$

$$\leq |a_{11} + a_{12} + \dots + a_{1J}| + |a_{21} + a_{22} + \dots + a_{2J}| + \dots + |a_{I1} + a_{I2} + \dots + a_{IJ}| \quad (\text{A.27})$$

$$= \left| \sum_{j=1}^J a_{1j} \right| + \left| \sum_{j=1}^J a_{2j} \right| + \dots + \left| \sum_{j=1}^J a_{Ij} \right| \quad (\text{A.28})$$

$$= \sum_{i=1}^I \left| \sum_{j=1}^J a_{ij} \right| \quad (\text{A.29})$$

This leads to the following

$$\left| \sum_{i=1}^I \sum_{j=1}^J a_{ij} \right| \leq \sum_{i=1}^I \left| \sum_{j=1}^J a_{ij} \right| \quad (\text{A.30})$$

A.3.2 Reordering of the square of a sum

$$\left(\sum_{i=1}^n a_i \right)^2 = (a_1 + a_2 + a_3 + \dots + a_n)^2 \quad (\text{A.31})$$

$$\begin{aligned} &= a_1^2 + a_1 a_2 + a_1 a_3 + \dots + a_1 a_n \\ &\quad + a_2^2 + a_2 a_1 + a_2 a_3 + \dots + a_2 a_n \\ &\quad + \dots \\ &\quad + a_n^2 + a_n a_1 + a_n a_2 + \dots + a_n a_{n-1} \end{aligned} \quad (\text{A.32})$$

$$= \sum_{i=1}^n a_i^2 + 2 \sum_{i=1}^{n-1} \sum_{j=i+1}^n a_i a_j \quad (\text{A.33})$$

A.4 Relations Between Averaging, |1D FT|² and |2D FT|²

Case 3 is defined as performing 1D Fourier transform, then calculating absolute value and square of the variables followed by averaging. Case 4 performs the same calculations, but uses 2D Fourier transform instead of 1D.

Case 3 can be expressed as

$$G_3(k_x) = \frac{1}{N'} \sum_{i=1}^{N'} \left[\left| \sum_{x=0}^{M-1} s(x, z_i) e^{-j2\pi \frac{k_x x}{M}} \right|^2 \right] \quad (\text{A.34})$$

$$= \frac{1}{N'} \sum_{i=1}^{N'} |S(k_x, z_i)|^2 \quad (\text{A.35})$$

where $S(k_x, z_i) = \mathcal{F}_x\{s(x, z_i)\}$. Case 4 can be expressed as

$$G_4(k_x) = \frac{1}{N'} \sum_{i=1}^{N'} \left[\left| \sum_{x=0}^{M-1} \sum_{z=0}^{N-1} s(x, z_i) e^{-j2\pi \left(\frac{k_x x}{M} + \frac{k_z z}{N} \right)} \right|^2 \right] \quad (\text{A.36})$$

$$= \frac{1}{N'} \sum_{i=1}^{N'} |S(k_x, k_{z_i})|^2 \quad (\text{A.37})$$

where $S(k_x, k_{z_i}) = \mathcal{F}_{x,z}\{s(x, z_i)\}$. Parseval's theorem states that

$$\int_{-\infty}^{\infty} |x(t)|^2 dt = \int_{-\infty}^{\infty} |X(f)|^2 df \quad (\text{A.38})$$

where $X(f) = \mathcal{F}\{x(t)\}$. When discrete Fourier transform (DFT) is used, the equality becomes

$$\sum_{m=0}^{M-1} |x(m)|^2 = \frac{1}{M} \sum_{k=0}^{M-1} |X(k)|^2 \quad (\text{A.39})$$

The theorem states that the sum of the square of a function is equal to $\frac{1}{M}$ times the sum of the square of its transform. This means that averaging the power spectrum in space correspond to averaging the power spectrum in the spatial frequency domain. The $\frac{1}{M}$ constant arises from the definition of DFT given in Eq. A.1 and Eq. A.2. By renaming Parseval's theorem to our denotation, it becomes

$$\sum_{i=0}^{N'-1} |S(k_x, z_i)|^2 = \frac{1}{N'} \sum_{i=0}^{N'-1} |S(k_x, k_{z_i})|^2 \quad (\text{A.40})$$

Case 4 can now be written as

$$G_4(k_x) = \frac{1}{N'} \sum_{i=1}^{N'} |S(k_x, k_{z_i})|^2 \quad (\text{A.41})$$

$$= \sum_{i=1}^{N'} |S(k_x, z_i)|^2 \quad (\text{A.42})$$

$$= N' G_3(k_x) \quad (\text{A.43})$$

The normalized DFT is given in A.5 and A.6. By using these equations, Parseval's theorem becomes

$$\sum_{m=0}^{M-1} |x(m)|^2 = \sum_{k=0}^{M-1} |X(k)|^2 \quad (\text{A.44})$$

By denoting \hat{S} as the normalized Fourier transform of s , the power spectrum for case 3 when using normalized Fourier transform is

$$\hat{G}_3(k_x) = \frac{1}{N'} \sum_{i=1}^{N'} \left[\left| \frac{1}{\sqrt{M}} \sum_{x=0}^{M-1} s(x, z_i) e^{-j2\pi \frac{k_x x}{M}} \right|^2 \right] \quad (\text{A.45})$$

$$= \frac{1}{N'} \sum_{i=1}^{N'} \left| \hat{S}(k_x, z_i) \right|^2 \quad (\text{A.46})$$

where $\hat{S}(k_x, z_i) = \text{normalized } \mathcal{F}_x \{s(x, z_i)\}$.

$$\hat{G}_4(k_x) = \frac{1}{N'} \sum_{i=1}^{N'} \left[\left| \frac{1}{\sqrt{MN}} \sum_{x=0}^{M-1} \sum_{z=0}^{N-1} s(x, z_i) e^{-j2\pi \left(\frac{k_x x}{M} + \frac{k_z z}{N} \right)} \right|^2 \right] \quad (\text{A.47})$$

$$= \frac{1}{N'} \sum_{i=1}^{N'} \left| \hat{S}(k_x, k_{z_i}) \right|^2 \quad (\text{A.48})$$

where $\hat{S}(k_x, k_{z_i}) = \text{normalized } \mathcal{F}_{x,z} \{s(x, z_i)\}$. By using Parseval's theorem in Eq. A.44, the lateral power spectrum for case 4 becomes

$$\hat{G}_4(k_x) = \frac{1}{N'} \sum_{i=1}^{N'} \left| \hat{S}(k_x, k_{z_i}) \right|^2 \quad (\text{A.49})$$

$$= \frac{1}{N'} \sum_{i=1}^{N'} \left| \hat{S}(k_x, z_i) \right|^2 \quad (\text{A.50})$$

$$= \hat{G}_3(k_x) \quad (\text{A.51})$$

Appendix B

GUI for Image Analysis System

A simple GUI has been made in MATLAB to test the different scenarios mentioned in this thesis in addition to the imaging system from the project assignment. All MATLAB files can be found on the zip file attached in the electronic version of the thesis. By running the MATLAB file `menuSystem.m`, Figure B.1 is displayed. The user chooses to analyze a recorded image or a simulated image.

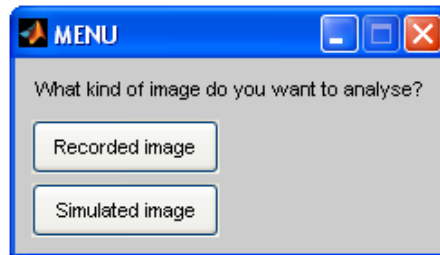
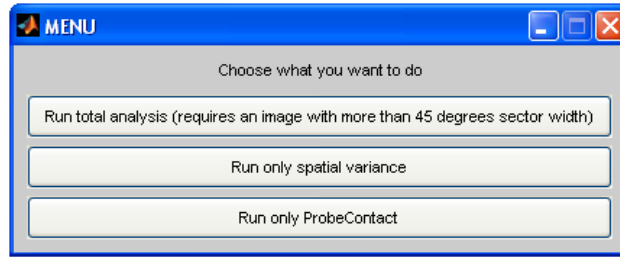
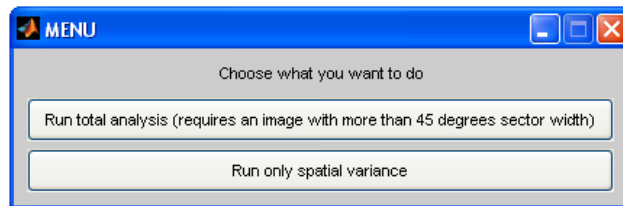


Figure B.1: First menu that appears when running `menuSystem.m`. The user gets the option to analyze a recorded image or a simulated image. By pushing the “X” button in the upper right corner, no analysis will be performed.

If the user pushes the “Recorded image” button, Figure B.2(a) will appear, and if the user pushes the “Simulated image” button, Figure B.2(b) will appear. The ProbeContact algorithm is not implemented for simulated images and is accordingly not a part of the menu in Figure B.2(b). If the button “Run total analysis (requires an image with more than 45 degrees sector width)” in the second menu is pushed, the image analysis system from the project assignment will start analyzing the image, followed by running the spatial variance algorithm and if it is a recorded image, the ProbeContact algorithm will evaluate the image in the end. The image analysis system does not only evaluate the point targets which are align vertical above each other, but also point targets further away from the center, and the image must minimum have a 45° sector width. If the button “Run only spatial variance” is pushed, only the spatial variance algorithm will evaluate the image. If the button “Run only ProbeContact” is pushed for the scanned image, only the ProbeContact algorithm will be executed.



(a) Second menu if the button "Recorded image" is chosen in first menu



(b) Second menu if the button "Simulated image" is chosen in first menu

Figure B.2: Second menu that appears when running `menuSystem.m`. The user gets the options "Run total analysis" and "Run only spatial variance" (and "Run only ProbeContact" if a scanned image was chosen in the first menu).

If total analysis or only spatial variance analysis is chosen for a scanned image, a new menu shown in Figure B.3(a) will appear. In this menu, different variables must be set. If the image includes MLAs, it is specified here. In addition, the desired spatial variance calculations is now set by typing 1 (for yes) and 0 (for no). The spatial variance algorithm will always analyze the spatial variance for different beam densities. The different calculation types which also can be chosen are calculation of spatial variance for speckle, for various point targets and from IQ-data. It is also possible to make a movie of the moving point target.

If a simulated image is chosen in the first menu, the menu shown in Figure B.3(b) rather than the one in Figure B.3(a) will appear. In addition to choosing different parameters, the file path for the location of the simulated image must be specified.

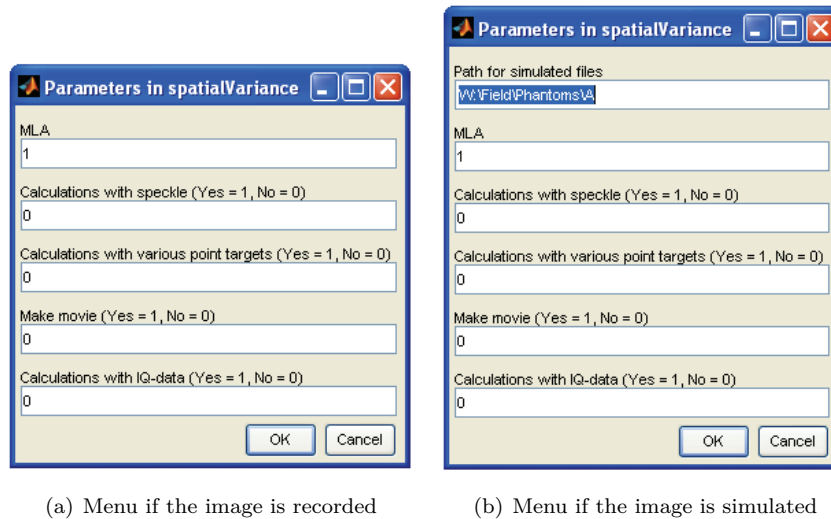


Figure B.3: Menu with options related to different types of calculations for spatial variance. The following must be set: number of MLAs, type of calculation related to speckle, various point targets and IQ-data, and whether making a movie of the point target.

Appendix C

Movie of Point Target

A movie of the point target discussed in Section 8.1.1 has been added to the zip file attached in the electronic version of the thesis. This movie is named `MovingPointTarget.avi` and is made in MATLAB.

The movie shows how a point target from a simulated image with 19 beams moves when the image is tilted to the side. Even though each frame is tilted with the same degree for every frame, the point target in the image will not move with equal distance.

Appendix D

Correlation Coefficient Calculations for IQ-data

A signal $s(x, z)$ can consist of

1. one single point target,

$$s_1(x, z) = A_1(x, z) h_{psf}(x, z|x_0, z_0) \quad (\text{D.1})$$

2. a sum of uncorrelated point targets,

$$\tilde{s}_n(x, z) = \sum_n s_n(x, z) = \sum_n A_n(x, z) h_{psf}(x, z|x_0, z_0) \quad (\text{D.2})$$

$h_{psf}(x, z|x_0, z_0)$ is the point spread function, and $A(x, z)$ is the strength of the point target and can be seen as a scaling variable.

Eq. 3.3 expresses the correlation with lag 0. By applying that $x[n] = s(x, z)$ and $y[n] = s(x + \Delta x, z + \Delta z)$, the correlation for our signal $s(x, z)$ with lag 0 can be expressed as

$$R = \langle s(x, z) s^*(x + \Delta x, z + \Delta z) \rangle \quad (\text{D.3})$$

For a single point target, the correlation is

$$R_1 = \langle s_1(x, z) s_1^*(x + \Delta x, z + \Delta z) \rangle \quad (\text{D.4})$$

$$= \langle A_1(x, z) h_{psf}(x, z|x_0, z_0) A_1^*(x + \Delta x, z + \Delta z) h_{psf}^*(x + \Delta x, z + \Delta z|x_0, z_0) \rangle \quad (\text{D.5})$$

$$= \langle A_1(x, z) A_1^*(x + \Delta x, z + \Delta z) h_{psf}(x, z|x_0, z_0) h_{psf}^*(x + \Delta x, z + \Delta z|x_0, z_0) \rangle \quad (\text{D.6})$$

For a sum of uncorrelated point targets, the correlation is

$$R_2 = \langle \tilde{s}_n(x, z) \tilde{s}_n^*(x + \Delta x, z + \Delta z) \rangle \quad (D.7)$$

$$= \left\langle \left(\sum_{n_1} s_{n_1}(x, z) \right) \left(\sum_{n_2} s_{n_2}(x + \Delta x, z + \Delta z) \right)^* \right\rangle \quad (D.8)$$

$$= \left\langle \left(\sum_{n_1} A_{n_1}(x, z) h_{psf}(x, z|x_0, z_0) \right) \right. \quad (D.9)$$

$$\left. \cdot \left(\sum_{n_2} A_{n_2}(x + \Delta x, z + \Delta z) h_{psf}(x + \Delta x, z + \Delta z|x_0, z_0) \right)^* \right\rangle \quad (D.10)$$

$$= \left\langle \sum_{n_1} A_{n_1}(x, z) h_{psf}(x, z|x_0, z_0) \right. \quad (D.11)$$

$$\left. \cdot \sum_{n_2} A_{n_2}^*(x + \Delta x, z + \Delta z) h_{psf}^*(x + \Delta x, z + \Delta z|x_0, z_0) \right\rangle \quad (D.12)$$

By applying that the expected value of two uncorrelated functions is zero and denoting that $\alpha = h_{psf}(x, z|x_0, z_0) h_{psf}^*(x + \Delta x, z + \Delta z|x_0, z_0)$, we get

$$\begin{aligned} R_2 &= \langle A_1(x, z) A_1^*(x + \Delta x, z + \Delta z) \alpha \\ &\quad + A_2(x, z) A_1^*(x + \Delta x, z + \Delta z) \alpha \\ &\quad + A_1(x, z) A_2^*(x + \Delta x, z + \Delta z) \alpha \\ &\quad + A_2(x, z) A_2^*(x + \Delta x, z + \Delta z) \alpha \\ &\quad + \dots + A_{n_1}(x, z) A_{n_2}^*(x + \Delta x, z + \Delta z) \alpha \rangle \end{aligned} \quad (D.13)$$

$$\begin{aligned} &= \langle A_1(x, z) A_1^*(x + \Delta x, z + \Delta z) \alpha \\ &\quad + \underbrace{\langle A_2(x, z) A_1^*(x + \Delta x, z + \Delta z) \alpha \rangle}_{\langle A_2(x, z) A_1^*(x + \Delta x, z + \Delta z) \rangle \cdot \alpha = 0 \cdot \alpha = 0} \\ &\quad + \underbrace{\langle A_1(x, z) A_2^*(x + \Delta x, z + \Delta z) \alpha \rangle}_{\langle A_1(x, z) A_2^*(x + \Delta x, z + \Delta z) \rangle \cdot \alpha = 0 \cdot \alpha = 0} \\ &\quad + \langle A_2(x, z) A_2^*(x + \Delta x, z + \Delta z) \alpha \rangle \\ &\quad + \dots + \langle A_{n_1}(x, z) A_{n_2}^*(x + \Delta x, z + \Delta z) \alpha \rangle \end{aligned} \quad (D.14)$$

$$= \left\langle \sum_n A_n(x, z) A_n^*(x + \Delta x, z + \Delta z) h_{psf}(x, z|x_0, z_0) h_{psf}^*(x + \Delta x, z + \Delta z|x_0, z_0) \right\rangle \quad (D.15)$$

$$= \left\langle \sum_n s_n(x, z) s_n^*(x + \Delta x, z + \Delta z) \right\rangle \quad (D.16)$$

It is assumed that $s_1(x, z)$ is normal distributed and this leads to that $s_n(x, z)$ is also so. Since $s_n(x, z)$ and $s_n(x + \Delta x, z + \Delta z)$ are normal distributed, the sum of $s_n(x, z)$ and $s_n(x + \Delta x, z + \Delta z)$ will also be normal distributed. This sum can be redefined as a new normal distributed function $\hat{s}(x, z)$.

When calculating the normalized correlation coefficient, the mean is first subtracted from the signal and this is then divided by the standard deviation.

By doing so, the coefficient is standardized. Standardizing a normal distribution makes all normal distributions into a single distribution with mean 0 and standard deviation 1 [13]. This means that standardizing $s_1(x, z)$ will give the same distribution as when standardizing $\hat{s}(x, z)$. Normalized correlation coefficient will then give the same result for a single point target and for a sum of uncorrelated point targets.